

# Creating the Radius Gap without Mass Loss

Eve J. Lee,<sup>1,2</sup>★ Amalia Karalis,<sup>1,2</sup> and Daniel P. Thorngren<sup>2,3</sup>

<sup>1</sup>*Department of Physics and McGill Space Institute, McGill University, Montréal, Québec, H3A 2T8, Canada*

<sup>2</sup>*Institute for Research on Exoplanets (iREx), Montréal, Québec, Canada*

<sup>3</sup>*Department of Physics, University of Montréal, Montréal, Québec, Canada*

Accepted XXX. Received YYY; in original form ZZZ

## ABSTRACT

The observed exoplanet population features a gap in the radius distribution that separates the smaller super-Earths ( $\lesssim 1.7R_{\oplus}$ ) from the larger sub-Neptunes ( $\sim 1.7\text{--}4R_{\oplus}$ ). While mass loss theories can explain many of the observed features of this radius valley, it is difficult to reconcile them with a potentially rising population of terrestrials beyond orbital periods of 30 days. We investigate the ability of initial gas accretion to reproduce both the location of the observed radius gap and the existence of long-period terrestrials. We first update the analytic scalings of gas accretion rate accounting for the shrinking of the bound radius by hydrodynamic effects. From the cooling evolution of planetary envelope with realistic opacity and equation of state, we find that the envelope mass fraction depends only weakly with the radius shrinking factor ( $M_{\text{gas}}/M_{\text{core}} \propto f_R^{0.31}$ ). Co-evolving planetary masses and disk structures, focussing on dust-free opacity, we find that gas accretion alone is able to carve out the observed radius gap, with slopes  $R_{\text{gap}} \propto P^{-0.11}$  and  $R_{\text{gap}} \propto M_{\star}^{0.24}$  for top-heavy; and  $R_{\text{gap}} \propto P^{-0.10}$  and  $R_{\text{gap}} \propto M_{\star}^{0.21}$  for bottom-heavy core mass distributions, in good agreement with observations. Our model reconciles the location of the radius gap with the existence of long period terrestrials. The peaks and valleys in the radius distribution were likely set in place primordially while post-formation processes further tune the exoplanetary population. We provide potential observational tests that may be possible with PLATO and Roman Space Telescope.

**Key words:** planets and satellites: formation

## 1 INTRODUCTION

Out of all the detected exoplanets thus far, super-Earths and sub-Neptunes comprise the large majority, with approximately 30–50% of Sun-like stars harbouring at least one of these small planets within orbital periods of  $\sim 300$  days (e.g., [Fressin et al. 2013](#); [Petigura et al. 2013](#); [Burke et al. 2015](#); [Zhu et al. 2018](#)). From measurements of radii and masses alone, interior modeling shows degeneracy between different compositions of the envelope and the planetary cores, which made unclear where to draw the line between the scaled-up version of rocky Earth and the scaled-down version of gas-enveloped Neptune (e.g., [Rogers & Seager 2010](#)). [Rogers \(2015\)](#) proposed that the distinction should be made at around  $\sim 1.6R_{\oplus}$  beyond which some level of H/He-dominated gaseous layer is required to explain both the masses and radii of close-in *Kepler* planets. With a larger dataset and more precise measurements of stellar parameters, we now have clear observational evidence of the distinction between super-Earths and sub-Neptunes which are evinced by a clear gap in the radius and radius-period distributions (e.g., [Fulton et al. 2017](#); [Van Eylen et al. 2018](#)).

This radius valley is considered to be a signature of envelope mass loss whether by photoevaporation ([Owen & Wu 2013, 2017](#)) or by core-powered envelope mass loss ([Ginzburg et al. 2018](#); [Gupta & Schlichting 2019](#)). In these theories, all super-Earths begin as gas-enveloped sub-Neptunes, and those that are most susceptible to mass

loss (i.e., those with low gravity and close proximity to the star) shed their outer envelope, transforming into bare rocks. Both theories enjoy success in explaining many of the observed features of the radius gap including the location and the overall shape of the gap in both one-dimensional radius and two-dimensional radius-period distributions, as well as the shift of the gap with respect to host stellar mass. Where these two theories differ is the range of wavelengths of the stellar flux that matters. For photoevaporation, only the XUV spectrum is relevant whereas for core-powered envelope mass loss, it is the bolometric flux that is key. These differences will materialize in the dependence of the radius gap with respect to stellar mass at a fixed bolometric incident flux; unfortunately, current dataset is not big enough to test this ([Lloyd et al. 2020](#); [Rogers et al. 2021](#)).

Another potential way to distinguish between the two mass loss models is the system age. It is generally expected that photoevaporative mass loss carves out the gap in the first  $\sim 100$  Myrs when the stars remain active whereas core-powered envelope mass loss is expected to carve out the gap over a longer  $\sim \text{Gyr}$  timescale. There is observational evidence that the radius distribution shifts at a statistically significant level across Gyr timescales (e.g., [Berger et al. 2020](#); [David et al. 2021](#)). However, EUV luminosity is expected to decline more slowly compared to X-ray so that photoevaporative mass loss may operate over  $\sim \text{Gyrs}$  as well (e.g., [King & Wheatley 2021](#)).

The origin of the radius gap may be traced to an even earlier time. [Lee & Connors \(2021\)](#) proposed that even in the absence of mass loss, late-time gas accretion alone can carve out the observed radius gap. For every core mass at a given orbital period, there exists a

★ E-mail: evelee@physics.mcgill.ca

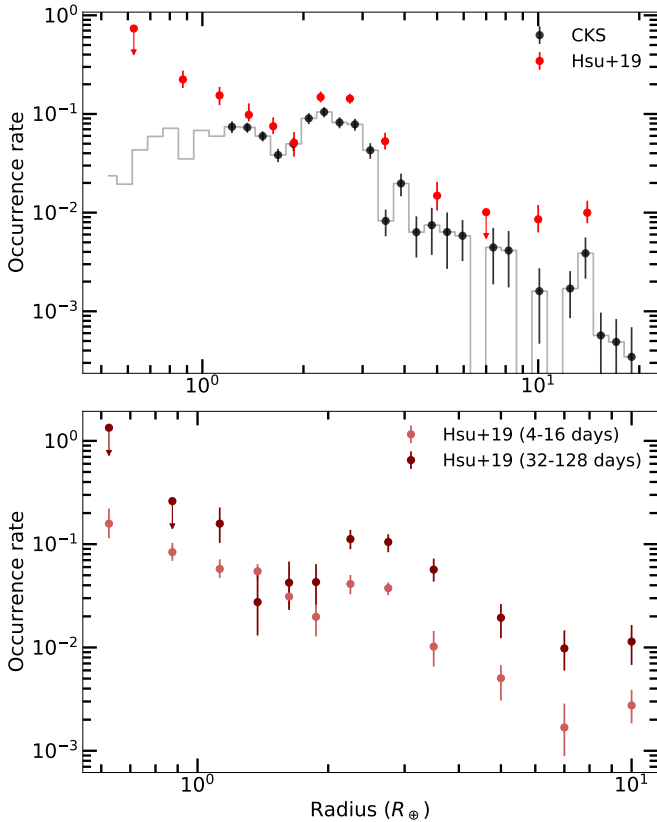


**Figure 1.** Top: Comparison of occurrence rates studies performed by California Kepler Survey (Fulton & Petigura 2018, <100 days; their Figure 5) and by Hsu et al. (2019, 2–64 days; their Table 2). The downward arrows denote upper limits. While the overall shape and the approximate location of the radius gap are similar between the two studies, Hsu et al. (2019) find an overall broader radius distribution both towards larger radii ( $> 3R_{\oplus}$ ) and smaller radii with a hint of mini-Earths ( $< R_{\oplus}$ ) becoming a dominant population. Bottom: Radius distribution at different orbital periods from Hsu et al. (2019). We verify their finding that there is no evidence of decrease in small planet ( $\lesssim 1.4R_{\oplus}$ ) population at long orbital periods.

maximum possible mass the core can accrete, set by the isothermal maximally cooled limit (Lee & Chiang 2015). Cores lighter than  $\sim 1\text{--}2M_{\oplus}$  (with the actual mass depending on orbital period) are so tiny that their isothermal limit attains envelope mass fraction of  $\lesssim 10^{-4}$ . With such tiny amount of gas, these planets’ radii are dominated by the size of their cores. The sharp drop of the expected envelope mass fraction below certain core masses manifests as a primordial gap in the radius and radius-period distribution with their location and shape consistent with what is currently observed.

One way to test the theory of primordial radius gap against mass-loss processes is to search for super-Earths beyond  $\sim 30$  days where both photoevaporation and core-powered envelope mass loss loses its potency and so these theories would expect no such planet at longer orbital periods.<sup>1</sup> There are already hints of the existence and dominance of super-Earths and mini-Earths beyond  $\sim 30$  days (Hsu et al. 2019, see also our Figure 1).

<sup>1</sup> Such prospect implies that current mass loss theories would predict solar system terrestrials to either not exist or be a secondary population (Owen & Wu 2017).

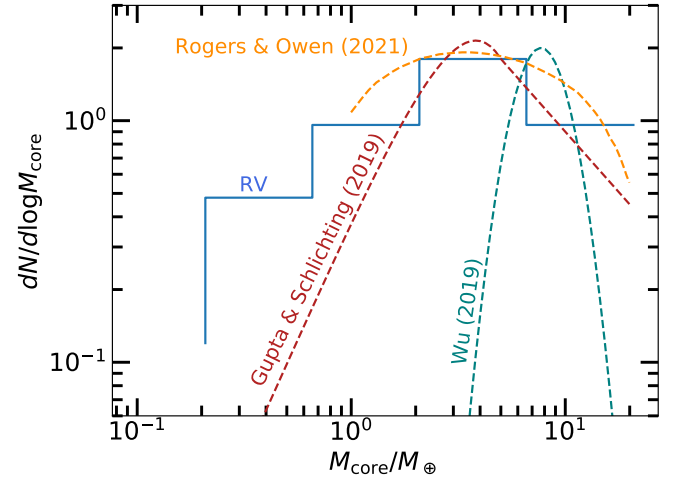


**Figure 2.** Best-fit core mass distributions of mass-loss models compared with the radial velocity follow-up of *Kepler* sub-Neptunes (RV, blue histogram) from Marcy et al. (2014). The RV distribution is not corrected for any observational biases. Wu (2019) assumes a lognormal core mass distribution and fits the photoevaporative mass loss model to the California Kepler Survey (CKS) radius distribution from Fulton & Petigura (2018). They find a distribution that is too peaked and shifted towards too high a core mass. Gupta & Schlichting (2019) assume a Rayleigh distribution for  $M_{\text{core}} < 5M_{\oplus}$  and  $dN/d\log M_{\text{core}} \propto M_{\text{core}}^{-1}$  for larger masses and fit the core-powered envelope mass loss model to the CKS data. Their lower mass tail falls off too sharply. Rogers & Owen (2021) consider a non-parametric form of  $dN/d\log M_{\text{core}}$  fitting the photoevaporative loss model to the CKS data, finding a much broader distribution. They still expect a fall-off at  $M_{\text{core}} < M_{\oplus}$ , which is hard to reconcile with the rise in small planets reported by Hsu et al. (2019); see also Figure 1.

Another advantage of the primordial radius gap is that it can accommodate broad core mass distributions. As shown in Figure 2, both mass loss theories predict a rather sharp and peaked core mass distribution which are either shifted toward too high a mass (Wu 2019) or too narrow (Gupta & Schlichting 2019) with respect to the radial velocity follow-up to *Kepler* planets (Marcy et al. 2014), even without correcting for a detection bias against small planets. Rogers & Owen (2021) obtain a much broader best-fit core mass distribution by using Bernstein polynomials to search for a non-parametric form of the distribution. They still expect a fall-off in the sub-Earth regime which is hard to reconcile with the lack of fall-off in the radius distribution at  $\lesssim 1R_{\oplus}$  in Hsu et al. (2019); see also Figure 1.

In this paper, we build on the work of Lee & Connors (2021) to investigate the emergence of the radius gap and its dependence on orbital period and host stellar mass using more realistic disk conditions. In particular, we are interested in more precise estimation of the disk temperature as the location of the primordial radius gap is sensitive to it. We will also benchmark our theory to the occurrence rate studies of Hsu et al. (2019) to determine the feasibility of reproducing the observed radius gap with a broad and potentially bottom-heavy core mass distribution without a peak.

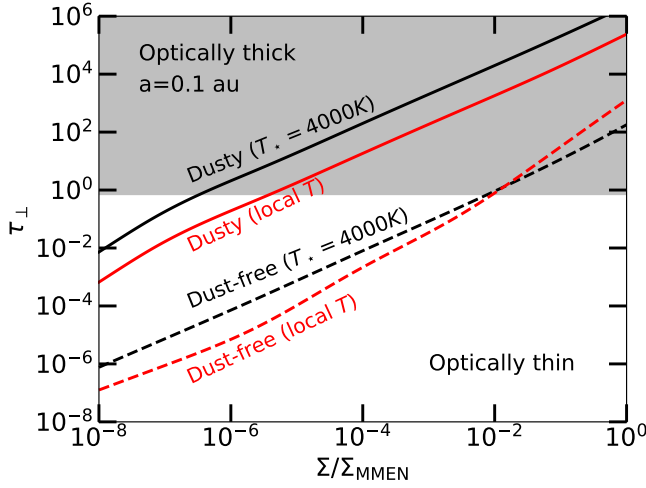


**Figure 3.** Vertical optical depth to stellar irradiation (black) and internal thermal radiation (red) vs. disk gas surface density, normalized to that of minimum mass extrasolar nebula (MMEN; Chiang & Laughlin 2013). When dust grains following the ISM grain size distribution dominate the opacity (solid lines), the disk remains optically thick at 0.1 au until the gas depletes by more than 6 orders of magnitude with respect to MMEN. When dust grains do not contribute to opacity (dashed lines), the disk becomes optically thin once the gas depletes by approximately 2 orders of magnitude. Sub-Neptune and super-Earth cores are expected to emerge once the disk gas depletes by  $\sim 3$ –4 orders of magnitude and so their gas accretion, if ‘dust-free’, will occur in disks optically thin to both incoming stellar light and outgoing thermal radiation.

## 2 METHODS

### 2.1 Disk Temperature

The isothermal maximum envelope mass is exponentially sensitive to the disk temperature at the location of the planetary core. In Lee & Connors (2021), we fixed the overall temperature profile to that of passive disks and let the normalization be a free parameter. Here, we derive more realistic disk temperature profiles.

First, we determine whether the disk is optically thin or thick to the incoming stellar light and outgoing thermal radiation. We compute the vertical optical depth through the disk to the incoming stellar irradiation and outgoing internal thermal radiation by integrating density and temperature-dependent Rosseland mean opacity over three vertical scale heights. The opacities are calculated using the methodology outlined in Section 2.2 of Lee et al. (2018). To summarize, we compute the Rosseland mean opacity to stellar irradiation  $\kappa_\star$  and internal thermal radiation  $\kappa_{\text{th}}$  by integrating wavelength-specific opacities  $\kappa$  generated from a modified version of the stellar atmosphere code PHOENIX as described in Ferguson et al. (2005), assuming solar metallicity ( $Z = 0.02$ , where elemental abundances are scaled to those in Grevesse & Noels (1993)). In ‘dusty’ models, metals take the form of dust grains following the interstellar medium (ISM) size distribution whereas in ‘dust-free’ models, metals are in the gas phase at their full abundances. Our choice of Ferguson et al. (2005) over Freedman et al. (2014) is motivated by the former’s inclusion of heavy atomic metals such as iron for more completeness. In calculating  $\kappa_\star$ , the Planck function is evaluated at the effective temperature of the host star (taken at 4000 K to be representative of pre-main sequence stars) whereas for  $\kappa_{\text{th}}$ , the Planck function is evaluated at the local temperature.

Typical masses of close-in sub-Neptunes are  $\lesssim 4\text{--}5M_\oplus$  (Marcy et al. 2014) which likely require a series of collisional mergers for their production.<sup>2</sup> Mass growth by mergers begins in earnest only in gas-poor environment—gas depletion of at least  $\sim 0.0005$  times the solar nebula—where the orbit-crossing timescale becomes comparable to the circularization timescale by gas dynamical friction (Kominami & Ida 2002; Lee & Chiang 2016). Similar levels of disk gas depletion are expected to explain the period ratio distribution of multi-planetary systems (Choksi & Chiang 2020).

Figure 3 demonstrates how disks with such severe gas depletion will be optically thin to both incoming stellar irradiation and outgoing internal thermal radiation when dust grains do not contribute to the overall opacity (‘dust-free’). When dust grains are the dominant sources of opacity, however, the disk remains optically thick down to  $\Sigma/\Sigma_{\text{MMEN}} \sim 10^{-6}$  (for internal radiation) and  $\sim 10^{-7}$  (for stellar irradiation), where  $\Sigma$  is disk gas surface density and  $\Sigma_{\text{MMEN}}$  is the gas surface density of minimum mass extrasolar nebula (Chiang & Laughlin 2013). In our discussion of planetary gas accretion, we provide expressions for both dusty and dust-free regimes for completeness. For our discussion of disk structure and our main results, we focus our attention on the dust-free regime and revisit dusty accretion in future work with a brief discussion in Section 4.3.

In general, the amount of total flux received from stellar irradiation dominates the dissipation flux from viscous accretion. It follows that if the disk is optically thin down to the midplane to both incoming and outgoing radiation, the midplane temperature is regulated by irradiation. We consider the trace amount of individual dust grains everywhere in the disk are being directly heated by the starlight and so they are heated to temperatures of

$$T_d^4 = \frac{L_\star}{16\pi\sigma_{\text{sb}}a^2\epsilon} \quad (1)$$

where  $L_\star$  is the luminosity of the central star,  $\sigma_{\text{sb}}$  is the Stefan-Boltzmann constant,  $a$  is the orbital distance, and  $\epsilon$  is the emissivity of the grains,  $\epsilon \propto T_d^\beta$  (e.g., Chiang & Goldreich 1997; Garaud & Lin 2007). We adopt the relevant temperature profile estimated by Chiang & Goldreich (1997):

$$T_d = 550 \text{ K} \left( \frac{a}{1 \text{ au}} \right)^{-2/5} \left( \frac{L_\star}{5.6 \times 10^{33} \text{ erg/s}} \right)^{1/5} \quad (2)$$

which assumes  $\beta = 1$ , yet, it is a close approximation of the more accurate solution found by Chiang et al. (2001, see their Figure 5). Since gas molecules are poor absorbers and emitters of optical and near infrared photons, we consider gas to be thermally equilibrated to the dust grains so that the disk temperature is set to  $T_d$  written in equation 2.

For stellar luminosities, we adopt the Johnstone et al. (2021) stellar evolution track which takes into account the full pre-main sequence stage evolution and the effect of stellar spin. For all our calculations, we adopt their median spin for a given stellar mass which derives from the measured rotation distributions of nearby young clusters. We note that in the timescales of our interest, our stars remain in their pre-main sequence phase and so their luminosities are larger, and the disk is hotter.

<sup>2</sup> While pebble isolation mass in sufficiently “turbulent” viscous disks ( $\alpha \gtrsim 0.01$ ) could attain these masses in the inner disk (e.g., Bitsch et al. 2018), it is not clear if disks are generally characterized by such high  $\alpha$ . In the outer disk, molecular line observations suggest that gas turbulence is generally weak (e.g., Flaherty et al. 2017, 2020).

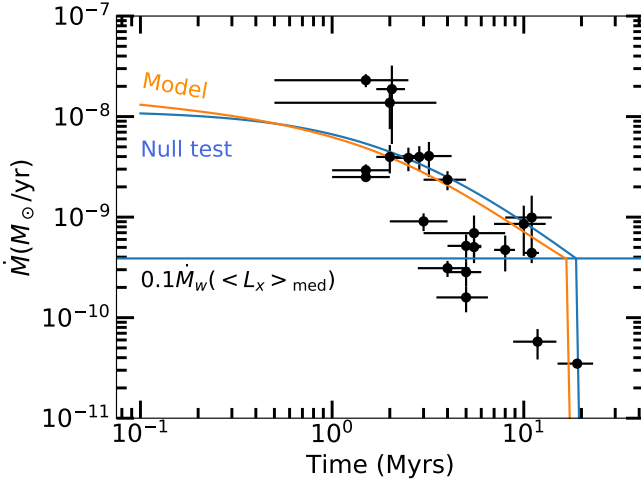


**Figure 4.** Expected accretion rate  $\dot{M}$  as a function of time under photoevaporation theory, drawing from young stellar object X-ray luminosities and disk fractions. See text for details of the calculation. The ‘Null test’ derives by fitting equations 5 and 6 to the datapoints (black circles). The ‘Model’ curve uses the best-fit parameters derived from the null test and includes the time evolution of disk temperature following the pre-main sequence evolution of the host star, contributing to the slight difference between the two curves. The rapid drop-off in disk accretion rate when it reaches 0.1 times the photoevaporative wind mass loss rate emulates the rapid draining of the inner disk once the latter decouples from the outer disk.

## 2.2 Disk Gas Surface Density

We consider a steady-state accretion disk of the form:

$$\Sigma_{\text{bg}}(a, t) = \begin{cases} 664 \left( \frac{a}{1 \text{ AU}} \right)^{-\frac{11}{10}} \left( \frac{t}{t_{\text{visc}}} + 1 \right)^{-\frac{14}{9}}, & t < t_{\text{dec}} \\ 664 \left( \frac{a}{1 \text{ AU}} \right)^{-\frac{11}{10}} \times \left( \frac{t_{\text{dec}}}{t_{\text{visc}}} + 1 \right)^{-\frac{14}{9}} \exp \left[ -\frac{(t-t_{\text{dec}})}{0.01 \times t_{\text{dec}}} \right], & t > t_{\text{dec}} \end{cases} \quad (3)$$

where  $t_{\text{visc}}$  is the characteristic viscous drift timescale and  $t_{\text{dec}}$  is the time at which the inner disk decouples from the outer disk via gap formation at  $\sim 2$  au due to photoevaporation. The choice of  $0.01 \times t_{\text{dec}}$  is motivated by the order of magnitude decrease in disk gas surface density at every 1% of disk lifetime post-gap formation found by Owen et al. (2011, see their Figure 9). Note that the first track ( $t < t_{\text{dec}}$ ) of equation 3 follows Lynden-Bell & Pringle (1974) and Hartmann et al. (1998) with the disk temperature  $T_d \propto a^{-2/5}$  (see equation 2).

The normalization of  $\Sigma_{\text{bg}}$  and the determination of  $t_{\text{visc}}$  and  $t_{\text{dec}}$  are guided by fitting a ‘null’ X-ray photoevaporation model to the observed X-ray luminosities of young stellar objects (YSOs) and the disk fraction of young star clusters, as outlined in Owen et al. (2011). To summarize, we first compute the X-ray luminosity function  $F_{L_x}$  of YSOs in Taurus from Güdel et al. (2007). For each young star clusters with measured disk fractions ( $f_d$ ; i.e., the fraction of member YSOs with infrared excess), we make an ansatz that  $f_d$  is the fraction of stars with X-ray luminosity smaller than  $F_{L_x}^{-1}(f_d) = L_c$ , under the assumption that the disk dispersal is dominated by X-ray photoevaporation. Numerical models of X-ray photoevaporation find that the disk begins to rapidly lose its gas when the photoevaporative mass loss rate becomes comparable to the global disk accretion rate (e.g., Owen et al. 2010). Using the relationship between the mass

loss rate  $\dot{M}_w$  by wind and X-ray luminosity, we can convert the observationally-inferred  $L_c$  into the disk accretion rate:

$$\dot{M}_{\text{acc}} = \dot{M}_w(L_c) = 6.4 \times 10^{-9} \left( \frac{L_c}{10^{30} \text{ erg/s}} \right)^{1.14} M_{\odot} \text{ yr}^{-1} \quad (4)$$

where we drop the correction factor  $A$  as it is expected to be 1 for primordial disks (Owen et al. 2011).

We compute the expected accretion rate vs. time using  $f_d$  and cluster age compiled by Mamajek (2009), complemented, where available, with updates from Michel et al. (2021), who used *Gaia* catalog to refine cluster member association and concluded that disks may be longer-lived than previously inferred. We also removed NGC 2024 and NGC 1333 from our analysis as their estimated ages are so small for their uncertainties that their lower limit would place their estimation at zero or negative. We fit to this data the expected form of  $\dot{M}_{\text{acc}}(t)$  based on our disk temperature profile:

$$\dot{M}_{\text{acc},1}(t) = \dot{M}_{\text{acc}}(0) \left( \frac{t}{t_{\text{visc}}} + 1 \right)^{-14/9} \quad (5)$$

for  $t < t_{\text{dec}}$  where  $t_{\text{dec}}$  is defined as  $\dot{M}_{\text{acc}}(t_{\text{dec}}) = 0.1\dot{M}_w(<L_x>_{\text{med}})$  with  $<L_x>_{\text{med}} = F_{L_x}^{-1}(0.5)$ . For  $t > t_{\text{dec}}$ ,

$$\dot{M}_{\text{acc},2}(t) = \dot{M}_{\text{acc},1}(t_{\text{dec}}) \exp \left[ -\frac{(t-t_{\text{dec}})}{0.01 \times t_{\text{dec}}} \right]. \quad (6)$$

We fit for  $\dot{M}_{\text{acc}}(0)$  and  $t_{\text{visc}}$  using the *emcee* package (Foreman-Mackey et al. 2013), obtaining  $\dot{M}_{\text{acc}}(0) = 0.94_{-0.40}^{+0.78} \times 10^{-8} M_{\odot} \text{ yr}^{-1}$  and  $t_{\text{visc}} = 2.78_{-1.00}^{+1.52}$  Myrs. Figure 4 shows the result of our ‘null’ test analysis, our best fit  $\dot{M}_{\text{acc}}(t)$ , and the full model that takes into account the time evolution of disk temperature due to stellar evolution, which makes  $\dot{M}(t)$  slightly steeper. For the full model,  $t_{\text{dec}} \sim 16.7$  Myrs. To convert  $\dot{M}(0)$  to the normalization of  $\Sigma_{\text{bg}}$ , we adopt the Shakura-Sunyaev parameter  $\alpha = 10^{-3}$ . Our disk becomes optically thin for dust-free opacity at  $t \gtrsim 3.5$  Myrs and so beyond this time, our expression for disk temperature in equation 2 is valid.

## 2.3 Core Mass, Assembly Time, and Orbital Period

How much envelope a planet ends up with depends sensitively on how massive their cores are and when the cores assemble (Lee 2019). From the radial-velocity follow-up of *Kepler* planets by Marcy et al. (2014), we infer that the underlying core mass distribution should drop beyond  $M_{\text{core}} \gtrsim 4-6 M_{\oplus}$ . Whether the distribution falls at lower masses or not is unclear at this point due to the difficulty in measuring low masses.

The bottom-heavy radius distribution of Hsu et al. (2019) for  $R \lesssim 2R_{\oplus}$  suggests a potentially bottom-heavy core mass distribution. From the radial velocity follow-ups, we see no sub-Neptunes or super-Earths more massive than  $\sim 20 M_{\oplus}$ ; furthermore, larger sub-Saturns and giants are approximately an order of magnitude less numerous than their smaller counterparts. Motivated by these observations, we assume a following core mass distribution

$$\frac{dN}{d \log M_{\text{core}}} \propto M_{\text{core}}^{\delta} \exp \left( -\frac{M_{\text{core}}}{M_{\text{break}}} \right) \quad (7)$$

where  $\delta$  and  $M_{\text{break}}$  are free parameters. The power-law index  $\delta$  can be positive (top-heavy) or negative (bottom-heavy) and  $M_{\text{break}}$  emulates a fall-off in the core mass distribution at high mass end.

We draw the core assembly time  $t_{\text{core}}$  from a lognormal distribution:

$$\frac{dN}{d \log t_{\text{core}}} = \frac{1}{\sigma_t \sqrt{2\pi}} \exp \left[ -\frac{(\ln t_{\text{core}} - \ln t_{\text{typ,c}})^2}{2\sigma_t^2} \right] \quad (8)$$



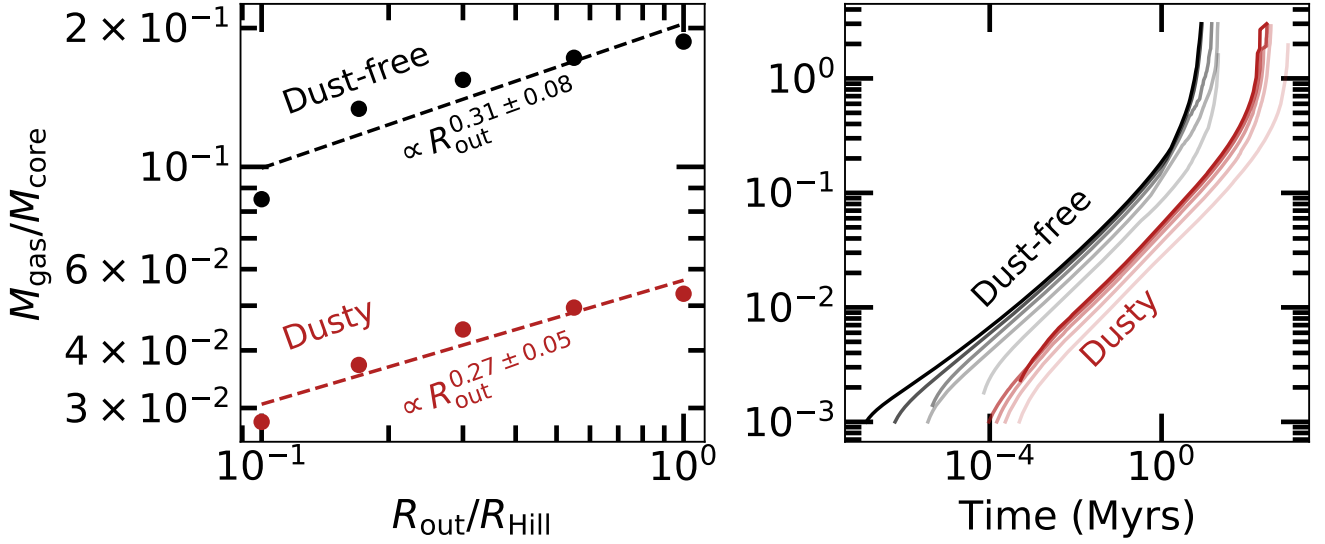


**Figure 5.** Envelope mass fraction of a  $5 M_{\oplus}$  core at 0.3 au in minimum mass extrasolar nebula, with its gas surface density reduced by a factor of 0.01. Left: how the final  $M_{\text{gas}}/M_{\text{core}}$  at 1 Myr scales with the outer boundary radius. We observe a weak dependence on the bound radius down to  $\sim 0.1 R_{\text{out}}/R_{\text{Hill}}$ . Right: time evolution of  $M_{\text{gas}}/M_{\text{core}}$  with lighter curves representing smaller  $R_{\text{out}}/R_{\text{Hill}} = (1.0, 0.55, 0.3, 0.17, 0.1)$ , as shown on the left panel.

where  $t_{\text{typ,c}}$  and  $\sigma_t$  are free parameters.

The occurrence rate of sub-Neptunes remains flat down to  $\sim 10$  days inside which they drop (Youdin 2011; Fressin et al. 2013; Petigura et al. 2018). The break at  $\sim 10$  days can be explained by the magnetospheric truncation of the underlying disk whose inner radii are expected to be at co-rotation radius with respect to their host star spin (Mulders et al. 2015; Lee & Chiang 2017). We draw the orbital periods  $P$  of our planets from the distribution

$$\frac{dN}{d \log P} \propto 1 - \exp \left[ - \left( \frac{P}{11.9 \text{ days}} \right)^{2.4} \right] \quad (9)$$

which follows closely the fitting result of Petigura et al. (2018) with a modification to enforce a log-uniform distribution of  $P$  beyond  $\sim 10$  days. Although planets larger than Neptune are observed to follow a different orbital period distribution, we adopt the above distribution uniformly across all our planets for simplicity.<sup>3</sup>

## 2.4 Gas Accretion

The rate at which a core accretes its gaseous envelope can be regulated by either cooling or hydrodynamic delivery (e.g., Pollack et al. 1996; Tanigawa & Tanaka 2016). We largely adopt the methodology of Lee (2019) in computing the envelope mass accreted onto our planet except we scale from the full numerical solution of Lee et al. (2014) and Lee & Chiang (2016) instead of approximating the runaway as an exponential growth. As the goal of this paper is to assess the entire radius distribution including the radius gap at  $\sim 1.8 R_{\oplus}$ , the rise of small terrestrials, and the cliff at  $\sim 3\text{--}4 R_{\oplus}$ , we need to properly account for the runaway growth. Here, we summarize the key points while highlighting the differences.

<sup>3</sup> Hallatt & Lee (2022) have shown that even if sub-Saturns initially follow a log-uniform period distribution, mass loss processes would erode short-period sub-Saturns into smaller planets, sculpting a monotonically increasing orbital period distribution that is currently observed.

### 2.4.1 Accretion by Cooling

We integrate the stellar structure equations 5–8 of Lee et al. (2014) from the bound radius of the envelope  $R_{\text{out}} = f_R \min(R_{\text{Hill}}, R_{\text{Bondi}})$ —where  $f_R$  is a numerical factor,  $R_{\text{Hill}}$  the Hill radius, and  $R_{\text{Bondi}}$  the Bondi radius—down to the inner boundary set at the core radius  $R_{\text{core}}/R_{\oplus} = f_{\rho_c}^{-1/3} (M_{\text{c}}/M_{\oplus})^{1/4}$  (Valencia et al. 2006), where  $f_{\rho_c}$  a numerical factor of core density with respect to that of the Earth. Compared to  $R_{\text{core}} \propto M_{\text{core}}^{1/3}$  used by Lee et al. (2014), this makes negligible difference in the envelope mass fraction but could lead to observable difference when translated to radius so we adopt the  $R_{\text{core}} \propto M_{\text{core}}^{1/4}$  scaling for more accuracy. At  $R_{\text{out}}$  the density and the temperature of the planet smoothly connects to that of the disk. We use the opacity tables built by the methodologies of Ferguson et al. (2005) and compute our own equation of state, as outlined in Lee et al. (2014).

Three-dimensional hydrodynamic calculations report  $f_R$  can be as low as 0.1–0.3 (Lambrechts & Lega 2017; Fung et al. 2019) as the advective flow of the disk can shrink the extent of the bound trajectory of gas around the planet. While some hydrodynamic simulations report complete recycling of gas or the advection alone completely limiting the envelope growth beyond a few percent by mass (e.g., Béthune & Rafikov 2019; Moldenhauer et al. 2021), these calculations are limited by their difficulty in resolving the innermost convective envelope whose mass is centrally concentrated (Lee et al. 2014) and therefore more likely to be shielded from the effects of the outer flow. Figure 5 demonstrates that the rate of envelope mass growth decreases with smaller bound radius but its effect is weak. First, this decrease can be explained by the steeper density profile and therefore more optically thick radiative-convective boundary (rcb) for smaller  $R_{\text{out}}$ . As Figure 6 illustrates, to pack the same amount of envelope within a smaller spatial extent, the density profile necessarily steepens and so the density and therefore the optical depth at the rcb rises. Since the rcb regulates the rate of cooling and therefore accretion, slower cooling begets slower accretion. The change in the density

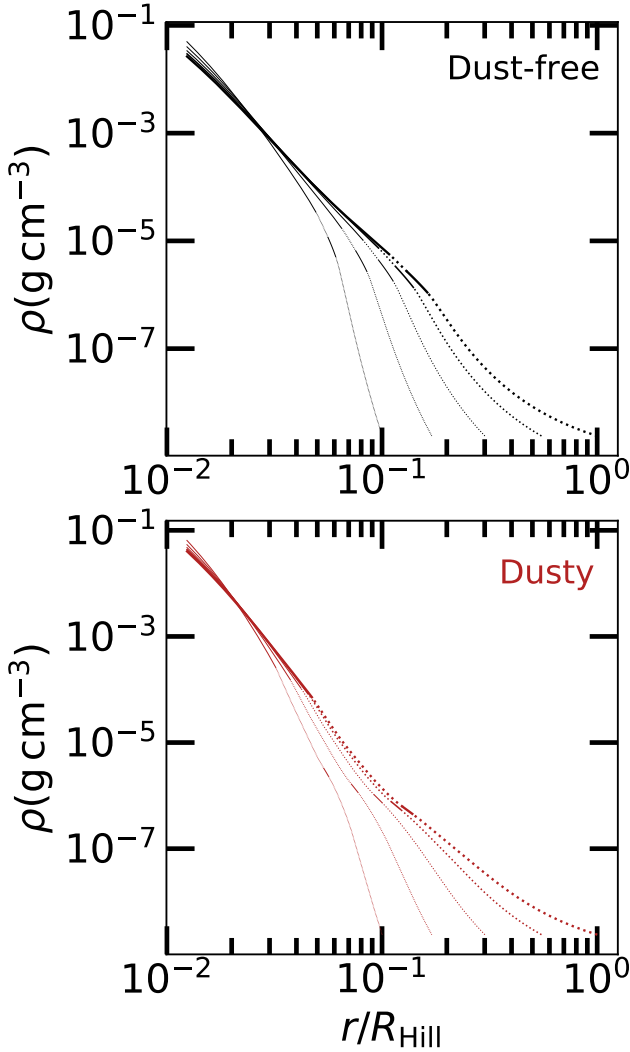


**Figure 6.** Radial density profiles of a  $5M_{\oplus}$  core at 0.3 au with  $M_{\text{gas}}/M_{\text{core}} = 0.01$ . The underlying disk is minimum extrasolar nebula with its gas depleted by a factor of 100. Like Figure 5, lighter curves represent smaller  $R_{\text{out}}/R_{\text{Hill}} = (1.0, 0.55, 0.3, 0.17, 0.1)$  while solid and dotted lines illustrate convective and radiative zones, respectively. The small convective windows are created by a small increase in opacities at temperatures of  $\sim 800$  K, likely corresponding to the water absorption line at  $\sim 3\mu\text{m}$ . Smaller  $R_{\text{out}}$  steepens the overall density profile, rendering the radiative-convective boundary (rcb) more optically thick. Yet, these differences are minimal unless the envelope shrinks below the original rcb (i.e., the rcb of  $R_{\text{out}}/R_{\text{Hill}} = 1$  case, which is  $\sim 0.1R_{\text{Hill}}$ ).

at the rcb however is only of order unity unless  $R_{\text{out}}$  shrinks below the initial location of the rcb which is  $\sim 0.1R_{\text{Hill}}$ ; this explains the noticeable drop in  $M_{\text{gas}}/M_{\text{core}}$  at  $R_{\text{out}}/R_{\text{Hill}} = 0.1$  in Figure 5. Even at  $R_{\text{out}}/R_{\text{Hill}} = 0.1$ , the envelope mass fraction still drops by factors of  $\lesssim 2$ .

Ali-Dib et al. (2020) showed that in disks with sufficiently high entropy (equivalent to high temperature and low density), advection of entropy into the deeper layers of the envelope can stall its mass growth by an erasure of the inner convective zone. Such behaviour can also be explained from the perspective of density steepening. For a fixed envelope mass, smaller disk gas density requires a steeper envelope density profile. This requirement is exacerbated by the en-

tropy advection which forces the outermost layer to be convective (i.e., shallower density profile) and only becomes worse if the penetration depth of the advective flow is assumed to be deeper. For high enough envelope mass, the solution to structure equations demands that the innermost profiles to be steep and therefore fully radiative. In our calculations, we always find the innermost convective zone except when the disk gas surface density drops by more than 8 orders of magnitude (Lee et al. 2018). We note that it is possible that the effect of entropy advection calculated in Ali-Dib et al. (2020) may be overestimated by their assumption of inner adiabatic index of  $\gamma = 7/5$  which creates an outwardly concentrated mass profile. Using more realistic opacities and equation of state, we obtain an inner adiabatic index of  $\gamma \sim 1.2$  due to the thermostat effect of hydrogen molecule dissociation (Lee et al. 2014), and this smaller  $\gamma < 4/3$  creates an inwardly concentrated mass profile, dulling any effect on the envelope structure by outer boundary conditions.

#### 2.4.2 Scaling to Different Cores and Disk Conditions

We use the analytic scaling relations found by Lee & Chiang (2015) to scale our numerical calculations of  $M_{\text{gas}}/M_{\text{core}}$  to a wide variety of core and disk properties. The scaling indices differ slightly due to our use of  $R_{\text{core}} \propto M_{\text{core}}^{1/4}$  instead of  $R_{\text{core}} \propto M_{\text{core}}^{1/3}$ . Since what changes is the rate of gas accretion and more specifically the cooling timescale, we apply scaling to the time, rather than  $M_{\text{gas}}/M_{\text{core}}$ . More technically speaking, we shift the time axis for our base  $M_{\text{gas}}/M_{\text{core}}(t)$  computed numerically for  $5M_{\oplus}$  core at 0.3 au ( $\rho_{\text{disk}} = 2.4 \times 10^{-9} \text{ g cm}^{-3}$ ,  $T_{\text{disk}} = 600$  K,  $R_{\text{out}}/R_{\text{Hill}} = 0.55$  for dust-free and 0.17 for dusty):

$$M_{\text{gas}}/M_{\text{core}} \propto t^{0.4} f_R^{0.31} T_d^{-1.5} Z^{-0.4} \mu_{\text{env}}^{2.2} M_{\text{core}}^{1.8} \Sigma_{\text{bg}}^{0.12} \\ t_{\text{scaled}} \propto t_{\text{base}} f_R^{-0.77} T_d^{3.75} Z \mu_{\text{env}}^{-5.5} M_{\text{core}}^{-4.5} \Sigma_{\text{bg}}^{-0.3}, \quad (10)$$

for dust-free, and

$$M_{\text{gas}}/M_{\text{core}} \propto t^{0.4} f_R^{0.28} Z^{-0.4} \mu_{\text{env}}^{3.4} M_{\text{core}}^{1.8} \Sigma_{\text{bg}}^{0.12} \\ t_{\text{scaled}} \propto t_{\text{base}} f_R^{-0.70} Z \mu_{\text{env}}^{-8.5} M_{\text{core}}^{-4.5} \Sigma_{\text{bg}}^{-0.3}, \quad (11)$$

for dusty, where  $Z$  is envelope metallicity and  $\mu_{\text{env}}$  is the mean molecular weight of the envelope. We solve for  $\mu_{\text{env}}$  self-consistently from an input  $Z$  which is set to solar metallicity 0.02 throughout this paper. The strong sensitivity of  $t_{\text{scaled}}$  on  $\mu_{\text{env}}$  is only relevant for high  $Z \gtrsim 0.2$ – $0.4$  (see Lee & Chiang 2016, their Figure 1). We note that the dust-free  $M_{\text{gas}}/M_{\text{core}}$  scales more strongly with  $M_{\text{core}}$  than what was used by Lee & Connors (2021). Such difference stems from the latter’s choice of using the “dust-free and gas-rich beyond 1 au” relation of Lee & Chiang (2015). We have verified numerically that  $M_{\text{gas}}/M_{\text{core}} \propto M_{\text{core}}^{1.8}$  is more correct in the parameter space of our interest (inside 1 au and gas-depleted). When computing the rate of gas accretion by cooling  $\dot{M}_{\text{cool}}$ , we numerically differentiate the base calculations, apply a Savitzky-Golay smoothing filter (from SciPy.signal) to avoid discontinuity due to numerical resolution, then interpolate the smoothed  $\dot{M}_{\text{cool}}$  with respect to  $t_{\text{scaled}}$  appropriately scaled for a given core and a given set of disk properties.

#### 2.4.3 Hydrodynamic Limit for Post-Runaway Planets

Once  $M_{\text{gas}}/M_{\text{core}} \sim 1$ , accretion by cooling enters the runaway phase triggered by thermal disequilibrium: large cooling power is required to keep massive envelopes in hydrostatic equilibrium which accelerates gas accretion requiring even larger cooling power, catastrophically shortening the cooling timescale. Once the runaway accretion

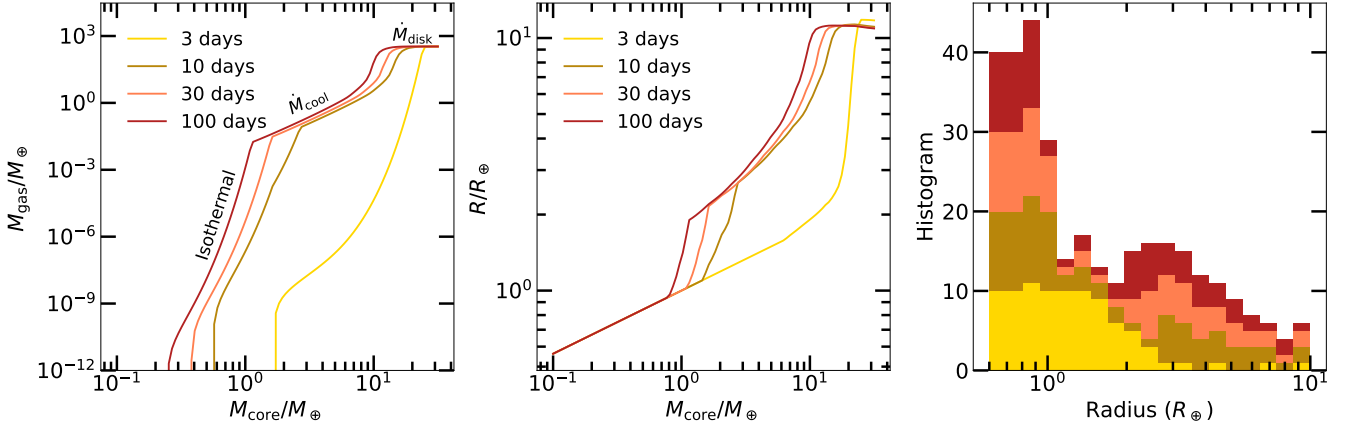


**Figure 7.** Left: Final envelope mass  $M_{\text{gas}}$  for dust-free accretion onto different core masses at various orbital periods around a solar mass star. All cores are assumed to have assembled at 14.5 Myrs and so have  $\sim 4.9$  Myrs to build their envelopes. For the most massive cores, their gas masses are determined by global disk accretion and so they all reach the same gas mass since disk accretion is independent of planet properties. Gas masses onto intermediate mass cores are determined by cooling. For the light cores, their  $M_{\text{gas}}$  is limited by the maximally cooled isothermal state which drops significantly at shorter orbital periods where the disk is hotter and therefore the Bondi radius is smaller. The lightest cores are unable to hold onto any gas ( $R_{\text{out}} < R_{\text{core}}$ ) and so we observe a precipitous drop. The slight change in the behaviour of isothermal  $M_{\text{gas}}$  vs.  $M_{\text{core}}$  across  $1.6M_{\oplus}$  at 10 days is due to the switch from  $R_{\text{out}} \propto R_{\text{Bondi}}$  to  $R_{\text{out}} \propto R_{\text{Hill}}$ . At orbital periods of 3 days, all cores with masses  $\lesssim 25M_{\oplus}$  have their gas masses limited by the isothermal state. Middle: corresponding radii, evaluated at 3 Gyrs, for the orbital period -  $M_{\text{gas}}$  -  $M_{\text{core}}$  depicted in the left panel. Right: the stacked distribution of planetary radii shown in the middle panel corresponding to each orbital period. Any sharp transition in gas mass and therefore radius vs. core mass brings about peaks and valleys in the radius distribution, even for an underlying core mass that is log-uniform. The transition from isothermal to cooling gas masses naturally creates a gap in the radius distribution at  $\sim 2R_{\oplus}$ . Another steep transition from cooling to disk accretion that arises from those that undergo runaway gas accretion accounts for the decrease in the number of planets  $\gtrsim 4R_{\oplus}$ .

is triggered, the rate of gas accretion is limited not by thermodynamics but rather by hydrodynamic delivery (e.g., Pollack et al. 1996) whether by local delivery or by global disk accretion, whichever provides smaller accretion rate. For the former, we adopt the equations 7 and 8 of Tanigawa & Tanaka (2016):

$$\dot{M}_{\text{hydro}} = 0.29 \left( \frac{M_p}{M_{\star}} \right)^{4/3} \Sigma_{\text{neb}} \left( \frac{a}{H} \right)^2 a^2 \Omega. \quad (12)$$

where  $M_p = M_{\text{core}} + M_{\text{gas}}$  is the total planet mass,  $M_{\star}$  the mass of the host star,  $H = c_{s,d}/\Omega$  the disk scale height,  $c_{s,d} = \sqrt{kT_d/\mu_d m_H}$  the disk sound speed,  $k$  the Boltzmann constant,  $\mu_d$  the disk mean molecular weight (calculated the same way as  $\mu_{\text{env}}$ ),  $m_H$  the mass of the atomic hydrogen,  $\Omega = \sqrt{GM_{\star}/a^3}$  the Keplerian orbital frequency,  $G$  the gravitational constant, and  $\Sigma_{\text{neb}} = \Sigma_{\text{bg}}/(1 + 0.034K)$  with

$$K = \left( \frac{H}{a} \right)^{-5} \left( \frac{M_p}{M_{\star}} \right)^2 \alpha^{-1}. \quad (13)$$

The depletion factor  $K$  represents the gap opening by the one-sided Lindblad torque of a planet against the viscous torque of the disk (e.g., Duffell & MacFadyen 2013; Fung et al. 2014). The scaling relationship of equation 12 can be understood as the shock of accretional flow at the planet-disk interface for  $R_{\text{Hill}} > H$  (equivalently,  $R_{\text{Hill}} < R_{\text{Bondi}}$ ). This particular scaling is relevant for isothermal shocks. We note that for the parameters of our interest (inner disk that is gas-depleted), the shock cooling timescale is significantly shorter than the orbital time so that the isothermal shock approximation is valid (see Lee 2019, their equation 8). We also note that planets that trigger runaway are massive enough that their  $R_{\text{Hill}} > H$  (i.e., all our planets that enter post-runaway accretion are super-thermal in contrast to sub-thermal planets at wide orbits studied by Ginzburg & Chiang (2019)).

The global disk gas accretion is estimated assuming viscous accretion rate:

$$\dot{M}_{\text{disk}} = 3\pi\alpha c_{s,d} H \Sigma_{\text{bg}} \quad (14)$$

with  $\alpha = 10^{-3}$ . We assume all the gas that diffuses past the planet's orbit is accreted by the planet as found by hydrodynamic simulations (e.g., Lubow & D'Angelo 2006). In almost all the planets we model, the hydrodynamic limit is given by  $\dot{M}_{\text{disk}} < \dot{M}_{\text{hydro}}$ , equivalent to the consumption-limited regime discussed by Rosenthal et al. (2020).

#### 2.4.4 Isothermal Limit

All planetary cores at a given mass and given location in a disk have maximum possible envelope mass they can accrete, given by the maximally cooled isothermal limit (i.e., when the entire envelope thermally relaxes to the outer nebula and reach a full isothermal profile):

$$M_{\text{iso}} = 4\pi\rho_{\text{disk}} \int_{R_{\text{core}}}^{R_{\text{out}}} r^2 \text{Exp} \left[ \frac{GM_{\text{core}}}{c_{s,d}^2} \left( \frac{1}{r} - \frac{1}{R_{\text{out}}} \right) \right] dr, \quad (15)$$

where  $\rho_{\text{disk}} = \Sigma_{\text{bg}}/H$  is the volumetric disk gas density.

For small cores ( $\lesssim 1-2M_{\oplus}$ ), this isothermal limit is so small that they could never have been sub-Neptunes to begin with. The steep drop in the expected envelope mass fraction for these planets is the reason why we expect the radius gap to be set in place primordially.

#### 2.4.5 Implementation

We follow the steps outlined below to compute the envelope mass fraction:

- (i) For each core, check if the envelope radius is larger than the

core radius ( $R_{\text{out}} = f_R \min(R_{\text{Hill}}, R_{\text{Bondi}}) > R_{\text{core}}$ ). If not, we stop the calculation and give zero envelope mass to the planet (physically, this planet is unable to hold on to a bound envelope). Otherwise we proceed.

(ii) For each core with a bound envelope, we compute the maximal isothermal mass following equation 15.

(iii) We integrate  $dM_{\text{gas}}/dt = \min(\dot{M}_{\text{cool}}, \dot{M}_{\text{hydro}}, \dot{M}_{\text{disk}})$  from the time at which cores assemble  $t_{\text{core}}$  to when  $\Sigma_{\text{bg}}$  falls by more than 8 orders of magnitude as this is when the entire envelope becomes almost completely radiative and so their accretion stops (Lee et al. 2018). For our disk, this time is  $\sim 19.4$  Myrs. Calculation of  $\dot{M}_{\text{cool}}$  is found in Section 2.4.2;  $\dot{M}_{\text{hydro}}$  in equations 12 and 13; and  $\dot{M}_{\text{disk}}$  in equation 14.

The left panel of Figure 7 showcases the result of our gas accretion calculation. Within the parameter space of our interest, we observe three different tracks. For small cores ( $\lesssim 1-3M_{\oplus}$ , depending on the orbital period), their envelope masses are set by their maximal isothermal limit. Intermediate mass cores ( $1 \lesssim M_{\text{core}}/M_{\oplus} \lesssim 10$ ) reach their final gas mass via cooling whereas for larger cores, they trigger runaway but ultimately their growth halts via global disk accretion. At extremely short orbital periods, the transition between isothermal to cooling growth disappears as the maximum mass a planet can attain shrinks due to smaller Bondi radius.

Sharp transitions in gas mass translate directly into sharp transitions in radii vs. core masses. These transitions give rise to peaks and valleys in the final radius distribution even if the underlying core mass distribution is uniform. The right panel of Figure 7 shows a gap at  $\sim 2R_{\oplus}$  which originates from the isothermal-to-cooling transition without any mass loss. The location of this radius gap shifts towards smaller radii farther from the star, as the transition core mass shifts to smaller masses (see left panel of Figure 7). We also see a drop in the population of planets larger than  $\sim 4R_{\oplus}$  which originates from the cooling-to-disk transition where planets undergo runaway gas accretion. Although this drop could be sharpened if the dissolution of gas into the core is accounted for (e.g., Kite et al. 2019), the drop itself can be naturally explained by gas accretion alone. We detail our method of radius calculation in the next section.

## 2.5 Envelope Mass Fraction to Planetary Radius

To compute the radius of the modeled (proto-)planets as they form, we use the interior structure models of Thorngren et al. (2016). These solve the equations of hydrostatic equilibrium, mass conservation, and the equation of state (EOS) on a 1-dimensional grid. For the EOS, we use Chabrier et al. (2019) for the H/He envelope, Thompson (1990) for the rock portion of the core, and Lyon & Johnson (1992) for the iron portion; we assume an Earth-like 2-to-1 ratio of rock to iron in the core. To determine the specific entropy of the envelope, we use the Fortney et al. (2007) atmosphere models to estimate the heat escaping the planet interior through the atmosphere. In the case of extremely thin (and therefore optically thin) envelopes, this underestimates the cooling rate of the planet; fortunately, these objects' radii are dominated by the core, which is insensitive to temperature. The core is assumed to be isothermal, with the specific heat set to  $7.5 \times 10^6 \text{ erg g}^{-1} \text{ K}^{-1}$ . For fast computation, we assembled a grid of evolution model radii at 40 core masses between 0.3 and 60  $M_{\oplus}$ , 33 gas-to-core mass ratios between  $10^{-6}$  and 1000, 9 incident fluxes from 0.01  $F_{\oplus}$  to 100  $F_{\oplus}$  where  $F_{\oplus}$  is the flux received by Earth from the Sun, and 100 ages from 10 Myr to 10 Gyr.

There are parts of the grid where the radius calculation fails due to the lack of coverage by the H/He EOS (mainly low mass cores

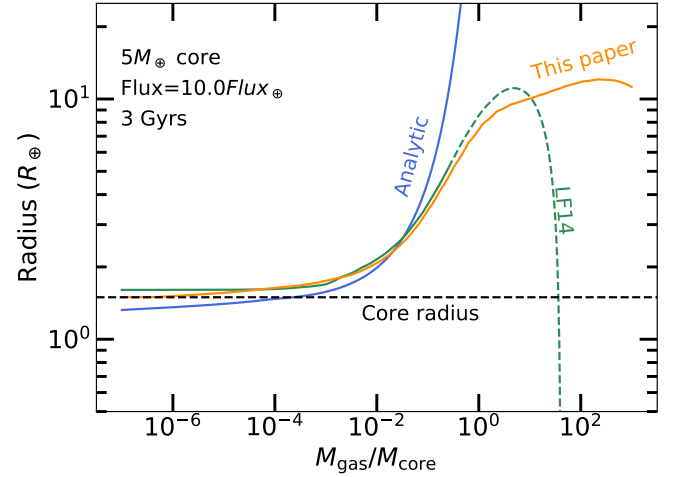


**Figure 8.** Comparison of radius conversion methods between the analytic scheme of Lee & Connors (2021, blue solid), extrapolating the grid of Lopez & Fortney (2014, green; LF14) and the grid presented in this paper (orange solid). The analytic scheme does not take into account the self-gravity of the envelope and therefore overestimates the radius at  $M_{\text{gas}}/M_{\text{core}} \gtrsim 0.1$ . LF14 grid only extends up to  $M_{\text{gas}}/M_{\text{core}} \sim 0.25$  (region covered by the grid plotted in solid; extrapolation in dashed) and so we see a failure in simple extrapolation for gas-dominated planets. Using the radius calculation presented in this work, we see a slight downturn in the radius at  $M_{\text{gas}}/M_{\text{core}} \sim 300$  (equivalent to  $\sim 5M_{\text{jup}}$ ) as we approach the brown dwarf regime.

with thin envelopes at late times). A simple extrapolation of the grid towards  $M_{\text{gas}}/M_{\text{core}} \ll 10^{-3}$  results in enlarged planetary radius even at these negligible envelope mass fraction. In order to smoothly connect the grid calculation to the radius of the bare core at very low envelope mass fractions, we stitch the analytic method outlined in Lee & Connors (2021), their Section 2.3, at  $M_{\text{gas}}/M_{\text{core}} \leq 10^{-3}$ , normalized to match the rest of the grid calculation.

In our analytic calculation of planetary radii, the envelope is assumed to have shrunk to a shell of convective gas with adiabatic index of 7/5 with a thin radiative atmosphere on top.<sup>4</sup> In order to make a correction for this atmosphere, we add to the radius of the rcb  $R_{\text{rcb}}$  the photospheric radius,

$$R_{\text{phot}} = \ln \left( \frac{\rho_{\text{rcb}}}{\rho_{\text{ph}}} \right) \frac{kT_{\text{eq}}}{\mu_{\text{atm}} m_H g} \quad (16)$$

where  $\rho_{\text{rcb}}$  is density at the rcb,  $\rho_{\text{ph}} = (2/3)\mu_{\text{atm}} m_H g / kT_{\text{eq}} \kappa$ ,  $\mu_{\text{atm}} = 2.374$  the atmospheric mean molecular weight,  $T_{\text{eq}}$  the equilibrium temperature,  $g = GM_{\text{core}}/R_{\text{rcb}}^2$  the surface gravity, and  $\kappa = 10^C \rho_{\text{rcb}}^\alpha (k/\mu_{\text{atm}} m_H)^\beta T_{\text{eq}}^{\alpha+\beta}$  is the opacity. We take  $C = -7.32$ ,  $\alpha = 0.68$ ,  $\beta = 0.45$  from Rogers & Seager (2010), which is appropriate for dust-free envelopes. Following the method of Lee & Connors (2021) obtains unphysically high  $\rho_{\text{rcb}} > 1 \text{ g cm}^{-3}$  for very thin envelopes (e.g., thinner than Earth atmosphere), which is a byproduct of enforcing a simple adiabatic structure. To avoid this, we take the minimum between the calculated  $\rho_{\text{rcb}}$  and the approximate

<sup>4</sup> We note that the adiabatic index of the inner envelope of our planets when they are accreting gas is different (and computed self-consistently using realistic equation of state) from 7/5 assumed here where planets are expected to have cooled down over  $\sim 0.1$ –few Gyrs.



calculation of the gas density at the bottom of the envelope:

$$\rho_{\text{bottom}} \sim \frac{M_{\text{gas}}}{4\pi R_{\text{rcb}}^2} \frac{g\mu_{\text{atm}}m_H}{kT_{\text{eq}}}. \quad (17)$$

We show in Figure 8 the result of this stitching as well as the comparison of the grid calculation presented here against the analytic calculation of Lee & Connors (2021) and the extrapolation of grid from Lopez & Fortney (2014).

## 2.6 Sample size and parameter limits

We now summarize the list of parameters that we vary in our model. The free parameters are the envelope bound radius  $f_R$  scaled to the minimum between the Bondi and the Hill radius, the power law slope  $\delta$  and the e-folding  $M_{\text{break}}$  that describe the underlying core mass distribution (equation 7), the median  $t_{\text{typ,c}}$  and the standard deviation  $\sigma_t$  of the core assembly time (equation 8), and the density of the planetary core  $f_{\rho_c}$  scaled to that of the Earth.

The potential dynamic ranges for  $f_R$  and  $f_{\rho_c}$  are narrow. Detailed hydrodynamic studies of Lambrechts & Lega (2017) and Fung et al. (2019) show that  $f_R \sim 0.2$ . Planets smaller than  $\sim 2R_{\oplus}$  with both mass and radii measurements are shown to be consistent with Earth composition with slight scatter (e.g., Dorn et al. 2019) so  $f_{\rho_c} \sim 1$ . The total number of free parameters then reduces to 4:  $\delta$  and  $M_{\text{break}}$  that describe that underlying core mass distribution and  $t_{\text{typ,c}}$  and  $\sigma_t$  that describe the distribution of core assembly times.

For each model ensemble, we draw 5000 core masses, orbital periods, and core assembly times from the distributions outlined in Section 2.3. Motivated by the radial velocity follow-up of *Kepler* planets by Marcy et al. (2014), we limit  $M_{\text{break}}$  to be between 3 and  $10 M_{\oplus}$ . We also limit  $-0.35 \leq \delta \leq 0.70$  whose lower limit is set by converting the radius distribution of  $R < 2R_{\oplus}$  of Hsu et al. (2019) into a core mass distribution (using  $R \propto M^{1/4}$  of Valencia et al. (2006) in the limit where these objects are mostly rocky planets) and whose upper limit is set by fitting a power-law to Marcy et al. (2014) for  $M \lesssim 4M_{\oplus}$ .

## 2.7 Comparison to observations

To search for the parameters that provide an acceptable agreement with the observed radius distribution, we compute the likelihood function in the cumulative distribution function (CDF) space:

$$\log \mathcal{L} = -\frac{1}{2} \sum_i \left[ \log \left( 2\pi\sigma_{\text{obs},i}^2 \right) + \frac{(C_{\text{model},i} - C_{\text{obs},i})^2}{\sigma_{\text{obs},i}^2} \right] \quad (18)$$

where  $C_{\text{model}}$  is the CDF of the model,  $C_{\text{obs}}$  is the CDF of the observed planetary occurrence rate,  $\sigma_{\text{obs}}$  is the  $1-\sigma$  observational error, and  $i$  iterates over different radii bin in Hsu et al. (2019) with measurements and errors (i.e., no upper limits). Both the model and the observed data are limited to  $0.75 \leq R/R_{\oplus} \leq 12$  and orbital periods of 5 and 64 days to make use of as many datapoints as possible. We note that in computing the final radii of model planets, we set their final age to 3 Gyrs. We use CDF instead of probability distribution function (PDF) as the former is less sensitive to the relative total number of planets in the sample. A more accurate comparison in PDF would necessitate a creation of mock observation (e.g., Rogers & Owen 2021) which is beyond the scope of this paper.

In general, we can find an acceptable agreement between the model and the observed radii distribution for both top-heavy ( $\delta > 0$ ) and bottom-heavy ( $\delta < 0$ ) core mass distribution provided that  $M_{\text{break}}$

is larger for the latter and smaller for the former. The best agreement (i.e., within  $1-\sigma$  using the likelihood estimation) is found for  $(\delta, M_{\text{break}}) = (0.3, 3M_{\oplus})$  and  $(-0.1, 7M_{\oplus})$  so we limit our discussion to these two cases.

Our finding here differs from that of Lee & Connors (2021) who conclude that the underlying core mass distribution must be top-heavy for gas accretion alone to reproduce the observed radius distribution. Two choices we made in this paper lead to such difference.

First, we use Hsu et al. (2019) as the reference observational data instead of Fulton & Petigura (2018) where the former clearly prefers a bottom-heavy radius distribution (see Figure 1). The two studies differ in their sample of planet-hosting stars and the statistical methods used to correct for detection biases. Whereas the California Kepler Survey (CKS) (Fulton & Petigura 2018) is limited to stars with well-characterized spectra (Petigura et al. 2017), Hsu et al. (2019) use the entire *Kepler* sample augmented with stellar parameters from Gaia data release 2 (Gaia Collaboration et al. 2018). The inverse detection efficiency method used by Fulton & Petigura (2018) is reported to underestimate the occurrence rate near the sensitivity limit (Hsu et al. 2018; Zhu & Dong 2021). Here, the approximate bayesian computation employed by Hsu et al. (2019) is thought to provide more accurate estimates. However, Fulton & Petigura (2018) state they limited their analysis to a region of parameter space where the pipeline completeness exceeds 25%. While it is not immediately obvious which occurrence rate estimate is more “correct”, we adopt Hsu et al. (2019) to verify whether our theory of gas accretion can accommodate both bottom-heavy core mass distribution and the location of the radius gap. Second, we compare directly with binned histograms instead of smoothing by Gaussian kernel. The latter is known to smear out fine features such as the radius gap so we conclude it is more appropriate to compare the raw distributions.

## 3 RESULTS

### 3.1 Radius distribution

Figure 9 illustrates the effect of varying  $M_{\text{break}}$ ,  $t_{\text{typ,c}}$  and  $\sigma_t$  on the final radius distribution. In general, higher  $M_{\text{break}}$  and shorter  $t_{\text{typ,c}}$  tend to produce a top-heavy radius distribution as expected since cores that are more massive and assemble early will accrete more gas and emerge puffer. The effect of  $\sigma_t$  is more subtle but in general, broader  $\sigma_t$  tends to smear away gaps in the overall radius distribution as it samples a broader range of envelope mass fractions for a given core mass. We choose two fiducial sets of parameters based on their agreement with the observations (see the third row of Figure 9):  $(\delta, M_{\text{break}}/M_{\oplus}, t_{\text{typ,c}}/\text{Myrs}, \sigma_t) = (0.3, 3, 14.5, 0.25)$  for top-heavy and  $(-0.1, 7, 14.5, 0.25)$  for bottom-heavy core mass distribution.

The histogram of the final radii of both fiducial models are shown in Figure 10. As analyzed in the CDF space, both models reproduce the overall shape of the observed radius distribution including the valley at  $\sim 1.8R_{\oplus}$  and the overall fall-off beyond  $\sim 4R_{\oplus}$ , each of which can be explained by the isothermal-to-cooling transition and the cooling-to-disk accretion transition in gas mass accrued by planetary cores, respectively, as explained in Figure 7.

We observe a significant “carving” of the radius distribution between 1 and  $2 R_{\oplus}$  in both models with respect to the distribution of core radii. This deficit comes about from some of the cores heavier than  $\sim 1M_{\oplus}$  accreting enough gas to emerge larger than  $\sim 1.8R_{\oplus}$  (see the middle and the bottom panels of Figure 10). As shown in Figure 7, at orbital periods within  $\sim 100$  days,  $\sim 1M_{\oplus}$  is approximately the minimum mass of the core that can reach radius  $\sim 2R_{\oplus}$ .

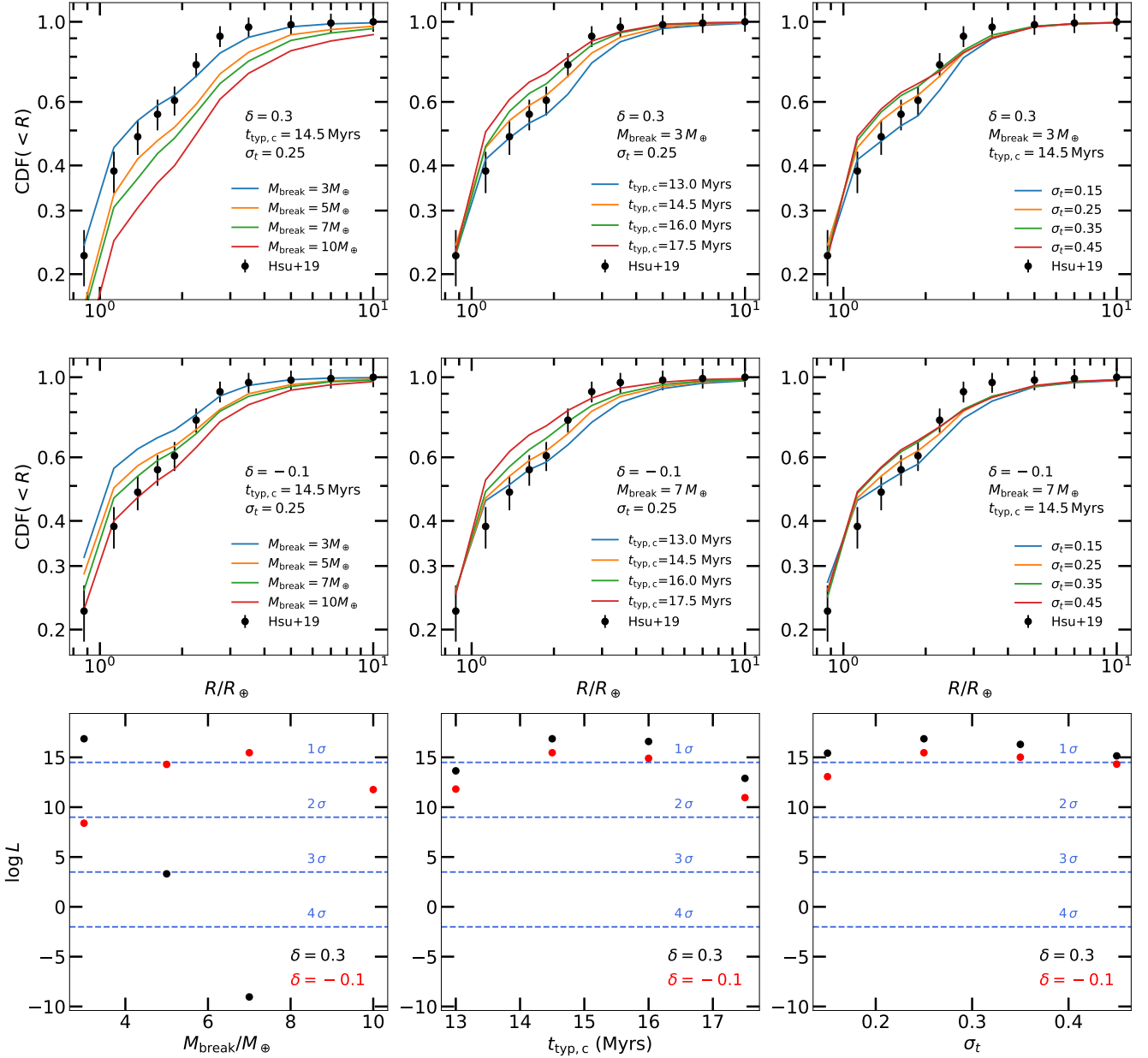


**Figure 9.** Cumulative distribution of planetary radii for our models and Hsu et al. (2019, Hsu+19). Top row: top-heavy core mass distribution ( $\delta = 0.3$ ). Middle row: bottom-heavy core mass distribution ( $\delta = -0.1$ ). Bottom row: log likelihood in cumulative distribution function comparing top-heavy and bottom-heavy core mass distribution models against Hsu et al. (2019). Based on the agreement with the data, we choose two fiducials:  $(\delta, M_{\text{break}}, t_{\text{typ},c}, \sigma_t) = (0.3, 3, 14.5, 0.25)$  for top-heavy and  $(-0.1, 7, 14.5, 0.25)$  for bottom-heavy core mass function.

### 3.2 Radius-Period Distribution

As demonstrated in Figure 11, both our top-heavy and bottom-heavy fiducial models reproduce the location and the overall morphology of the observed radius-period distribution of *Kepler* planets, including the “gap” that separates planets smaller than  $\sim 1.8R_\oplus$  from those larger. A more quantitative analysis is shown in Figure 12; by using the `gapfit` routine of Loyd et al. (2020), we obtain  $R_{\text{gap}} \propto P^{-0.11 \pm 0.01}$  for top-heavy and  $R_{\text{gap}} \propto P^{-0.10 \pm 0.01}$  for bottom-heavy models, both of which are within  $1\text{-}\sigma$  agreement with  $R_{\text{gap}} \propto P^{-0.09^{+0.02}_{-0.04}}$  reported by Van Eylen et al. (2018) and with  $R_{\text{gap}} \propto P^{-0.11 \pm 0.02}$  reported by Martinez et al. (2019). As described

in Lee & Connors (2021) the slightly decreasing  $R_{\text{gap}}$  with orbital period can be understood by the enlargement of the maximal isothermal mass limit for a given core mass farther from the star where the disk is colder. The primordial radius gap arises at the transition core mass between the isothermally-limited to envelope growth by cooling and so larger isothermal mass results in smaller transition core mass and therefore smaller  $R_{\text{gap}}$  (see also Figure 7).

While statistically our models are in agreement with the observations in 1-dimensional radius distribution, there are two noticeable differences in radius-period distributions. First, both our models feature a radius valley that is relatively “filled in” compared to obser-

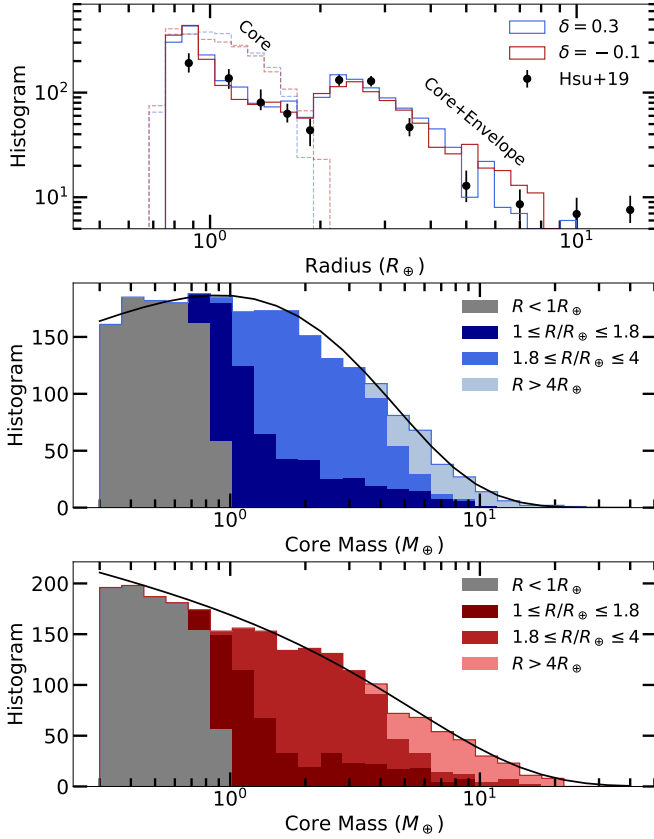


**Figure 10.** Top: radius histogram from Hsu et al. (2019, Hsu+19) compared to the two fiducial models. Both the final radii (solid) and that of the underlying cores (dashed) are plotted. Middle: stacked core mass histogram for the top-heavy fiducial model ( $\delta = 0.3$ ) broken down into different final radii. Bottom: same as the middle row but for the bottom-heavy fiducial model ( $\delta = -0.1$ ). For both middle and bottom panels, we overplot the analytic total core mass distribution from which the planets are drawn in black line.

variations as it is occupied by both bare rocky objects that are massive and gas-enveloped objects that are relatively light. With a broad distribution of core masses whose assembly times are independently determined, it is difficult to create a deep radius valley. It could be that the shape of the core mass distribution is more complex than what is assumed here and/or  $M_{\text{core}}$  and  $t_{\text{core}}$  are related; see more below.

Second, our bottom-heavy fiducial model overpredicts the number of gas giants ( $R > 8R_{\oplus}$ ) as compared to observations. Such overproduction is attributed to massive cores ( $M_{\text{core}} > 6M_{\oplus}$ ) that assembled relatively early and so had ample time to build their thick gaseous envelope. As hinted in Figure 7, with enough time, massive cores will undergo a brief period of runaway accretion before being limited by hydrodynamic effects such as the global disk accretion, which itself is high at early times. It is likely that the assembly time is mass-dependent with more massive cores requiring more time to be built up (e.g., Dawson et al. 2015). In the absence of first-principle understanding of the exact relationship between the assembly time and the core mass, we keep  $t_{\text{core}}$  and  $M_{\text{core}}$  as independent variables in this paper and revisit the history of core assembly in future studies.

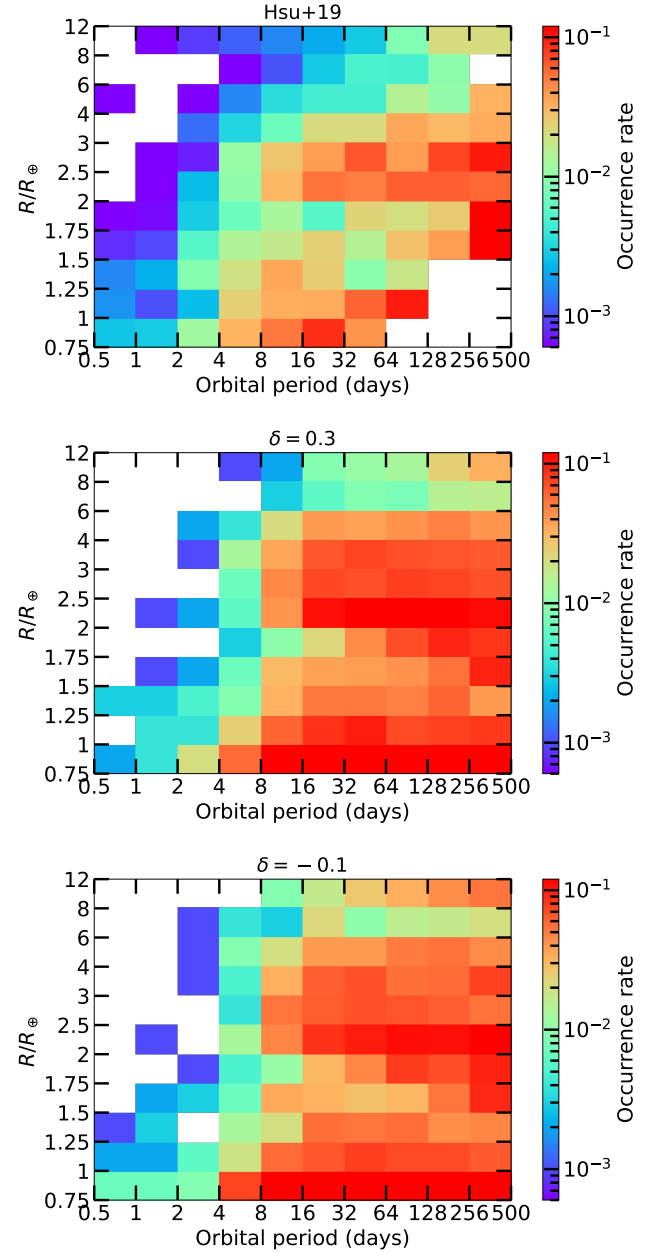


**Figure 11.** Planet occurrence rate over radius and period. Top: rates quoted by Hsu et al. (2019) based on a combined detection and vetting efficiency. Middle: from our top-heavy fiducial model population, whose amplitude is scaled by an arbitrary value for aesthetics. Bottom: same as the middle panel but for the bottom-heavy fiducial model. Both model populations recover much of the observed morphology including the general shape of the radius gap. The radius valleys in our models are shallower than that observed mainly due to our assumption of  $M_{\text{core}}$  and  $t_{\text{core}}$  being unrelated. Compared to the observational data, the bottom-heavy model features a noticeably larger population of  $8-12R_{\oplus}$  planets compared to  $6-8R_{\oplus}$  due to a set of massive cores with relatively short core assembly times.

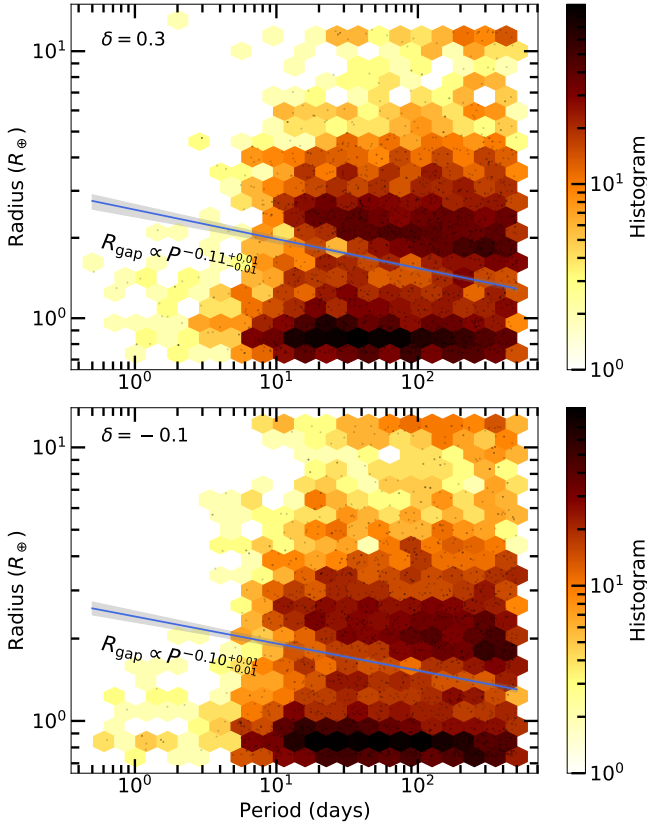


**Figure 12.** Two-dimensional histogram of the fiducial model planet population over radius and period. We use the `gapfit` routine of [Lloyd et al. \(2020\)](#) to calculate the best-fit location and the slope of the radius gap, annotated and illustrated here with a blue line with gray region outlining 1- $\sigma$  error.

### 3.3 Mass-Radius Distribution

In mass-radius space, our fiducial models produce two tracks (see Figure 13): the lower track corresponding to bare cores  $R \propto M^{1/4}$  and the upper track corresponding to gas-enveloped planets with the space between the two tracks sparsely populated. Currently, planets with both measured radii and masses fill in exactly this region of low population density. We note that the total number of confirmed planets with mass measurements is 226 compared to 3773 confirmed planets with radii measurements. It may be that with more mass measurements that can probe lighter planets, we may see real-life exoplanets filling in the upper track of the mass-radius phase space predicted by our dust-free gas accretion models.

Alternatively, it could be that the current mass-radii measurements are representative of the larger exoplanetary population. To reproduce the observed features purely from “dust-free” (i.e., dust grains are large enough they do not contribute to opacity) accretion of H/He-dominated gas onto silicate-Fe rocks, we need to set up a core mass distribution that is peaked at  $\sim 4\text{--}8M_{\oplus}$  with the core assembly time narrowly fine-tuned to  $\sim 17.5$  Myrs and cores larger than  $\sim 10M_{\oplus}$  assembled earlier  $\sim 16$  Myrs. Even if we make such fine-tuning to bring the model to a better agreement to the current observations in mass-radius space, it is difficult to reconcile the same model with the observed gap in the radius distribution that is as deep as what is seen in [Hsu et al. \(2019\)](#), even in 1-D radius distribution.

[Zeng et al. \(2019\)](#) have argued that the radius gap manifests in the

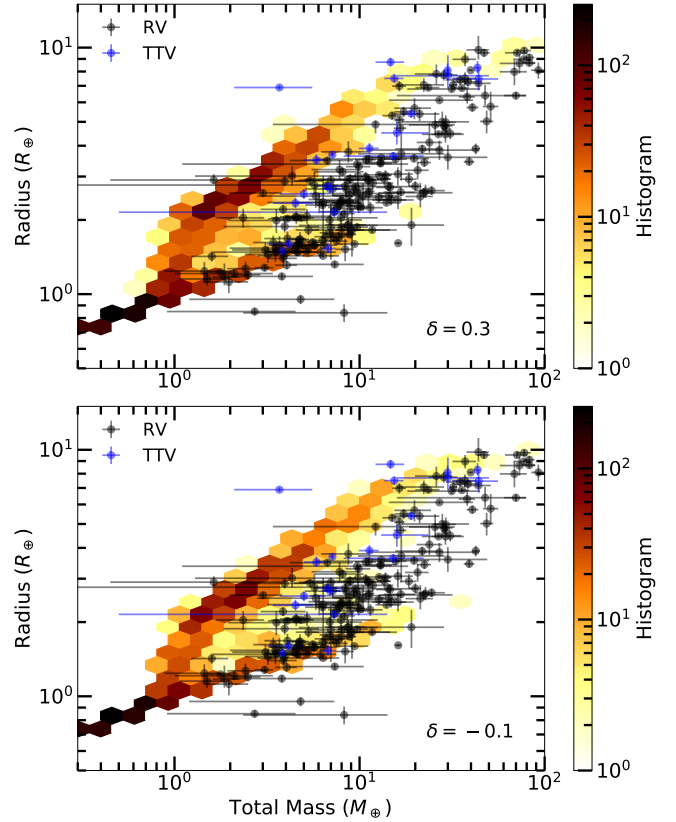


**Figure 13.** Mass-radius distribution of top-heavy and bottom-heavy fiducial models (coloured hexagonal histogram in the background) compared to measurements of confirmed planets (RV: black; TTV: blue) from NASA’s Exoplanet Archive downloaded December 29th of 2021. We limit both the observed dataset and the model to total mass  $\leq 100M_{\oplus}$ , orbital period  $\leq 64$  days, and radius  $\leq 10R_{\oplus}$ . Most planets lie within the region of the parameter space spanned by the model albeit in a sparsely populated space. One TTV measurement with radius well above the model population is Kepler-51 b ([Libby-Roberts et al. 2020](#)) which is a well-known super-puff. Its anomalously low density could be explained by its formation far away from the star ([Lee & Chiang 2016](#)), photochemical hazes in its upper atmosphere which enlarge the apparent radii ([Gao & Zhang 2020](#)), or circumplanetary rings ([Piro & Vissapragada 2020](#)).

mass-radius space separating  $\sim 1\text{--}10M_{\oplus} + \lesssim 2R_{\oplus}$  objects from  $\sim 3\text{--}20M_{\oplus} + \sim 2\text{--}3R_{\oplus}$  objects whereby the former represents silicate+Fe rocky terrestrials and the latter represents icy planets (see also [Venturini et al. 2020](#)). Interpreting the observed radius gap as a compositional dichotomy (of the planetary core) is hard to reconcile however with the observed trend between the location of the radius gap with orbital period/stellar insolation and stellar mass (e.g., [Berger et al. 2020](#)), and it may be that Earth-like cores with a large variety of H-atmosphere content suffice to explain the two distinct groups of planets that can be observed in the density space (see, e.g., [David et al. 2021](#), their Figure 21).

### 3.4 Radius-Stellar Mass

Around hotter (massive) stars, disks are hotter, so we expect the radius gap that emerges from primordial gas accretion to shift to a larger radius around hotter stars. Our expectation is corroborated in Figure 14 where we quantitatively solve for the location of the radius gap in



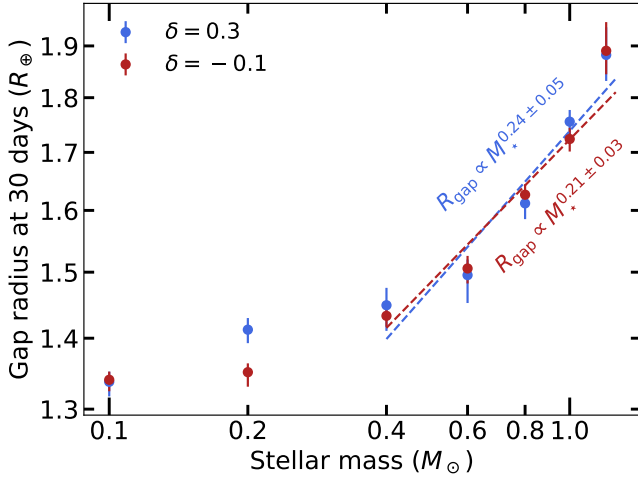


**Figure 14.** The location of radius gap evaluated at an orbital period of 30 days for each stellar mass. In general, the gap shifts to larger radii around more massive stars. The best-fit (fitted only within the range of stellar mass reported in Berger et al. (2020) for fair comparison) scaling relationship between the gap radius  $R_{\text{gap}}$  and the stellar mass  $M_{\star}$  for both top-heavy ( $\delta = 0.3$ ) and bottom-heavy ( $\delta = -0.1$ ) models agree with the measurement by Berger et al. (2020,  $R_{\text{gap}} \propto M_{\star}^{0.26+0.21}_{-0.16}$ ) within 1-sigma.

radius-period space (following the procedure outlined in Section 3.2) for model planet population around each stellar mass. A least-square fit finds that the shift in the gap radius with stellar mass is modest with  $R_{\text{gap}} \propto M_{\star}^{0.24 \pm 0.05}$  for the top-heavy ( $\delta = 0.3$ ) fiducial model and  $R_{\text{gap}} \propto M_{\star}^{0.21 \pm 0.03}$  for the bottom-heavy ( $\delta = -0.1$ ) fiducial model, both of which are in 1- $\sigma$  agreement with the measurement by Berger et al. (2020) who quote  $R_{\text{gap}} \propto M_{\star}^{0.26+0.21}_{-0.16}$ .

We note that the gap radius appears to shift more weakly with stellar mass at lower mass stars ( $\lesssim 0.4 M_{\odot}$ ). This change in behaviour arises from the location of the radius gap being set where the maximal isothermal gas mass limit crosses the cooling curve. The former is exponentially sensitive to the disk temperature whereas the latter scales slightly superlinearly with respect to the disk temperature (equation 10). It follows that the intersection between the two would appear at approximately the same envelope mass fraction (and therefore radii) at colder temperatures and start to deviate more strongly at higher temperatures.

## 4 DISCUSSION

### 4.1 Effect of mass loss

Although gas accretion alone is able to reproduce the observed radius gap, it is likely that some planets, especially those at short orbital periods, undergo post-accretion mass loss, further sculpting the exoplanet radius distribution. In fact, observations suggest a change in the radius distribution of exoplanets across  $\sim 1$ –2 Gyrs (e.g., Berger et al. 2020; David et al. 2021).

The two of the most well-established mass loss processes are photoevaporation (e.g., Owen & Wu 2013) and core-powered mass loss (e.g., Ginzburg et al. 2018). The former is often computed using energy-limited prescription corrected for some efficiency factor which encapsulates the complex relationship between the actual rate

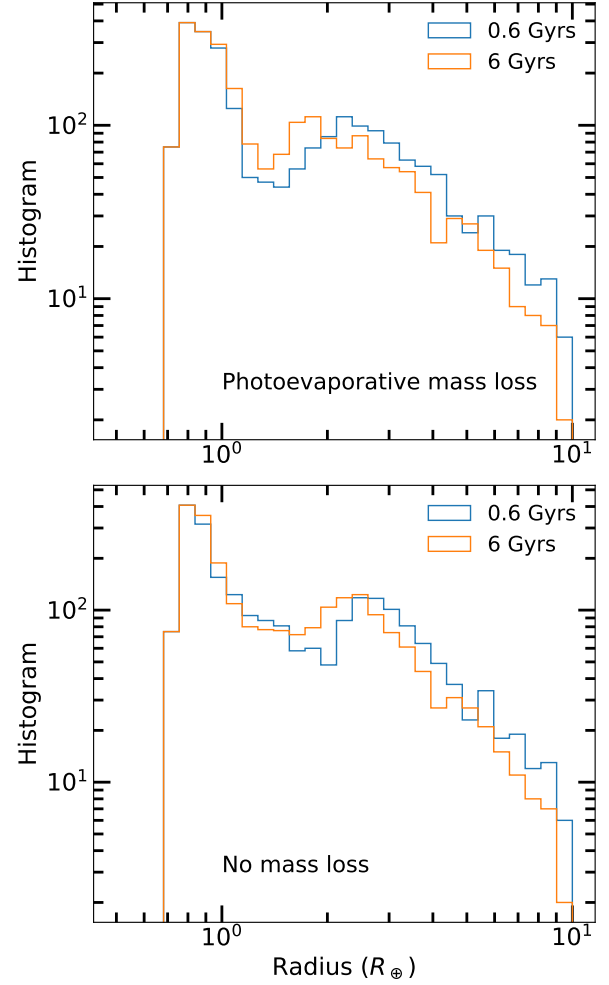


**Figure 15.** Radius distribution with photoevaporative mass loss (top) and without any mass loss (bottom), using the same initial envelope mass fraction computed for the bottom-heavy fiducial model ( $\delta = -0.1$ ). We see a shift in the local peak of the radius distribution in either scenario with mass loss models additionally filling in the  $\lesssim 1.4 R_{\oplus}$  end of the initial gap over time.

of mass loss with the degree of radiation and the gravitational potential of the planet (e.g., Owen & Jackson 2012) as well as the potentially drastic changes in the geometry of the outflow with planetary magnetic fields (e.g., Owen & Adams 2019). In core-powered mass loss, the outflowing wind is driven by the cooling of the core which heats up the envelope. While energetically the thermal inertia within the core can be enough to lift the entire gaseous envelope, the rate at which the core energy can be liberated depends on the composition and the viscosity of the core as well as the internal structure of the deeper layers of the envelope including condensation that can throttle planetary cooling for over  $\gtrsim 10$  Gyrs (S. Markham, private communication). Here, we will focus on the effect of photoevaporative mass loss.

Starting from the bottom-heavy ( $\delta = -0.1$ ) fiducial model, we evolve planetary radii with and without mass loss. For mass loss, we use the following formula:

$$\dot{M} = -\eta \frac{\pi R_p^3 F_{\text{XUV}}}{GM_p} \quad (19)$$

where  $\eta$  is the efficiency factor,  $R_p$  is planetary radius using the

conversion method we described in Section 2.5,  $F_{\text{XUV}}$  is XUV flux computed using the evolutionary track of [Johnstone et al. \(2021\)](#),  $G$  is the gravitational constant, and  $M_p$  is the total planetary mass. To account for varying  $\eta$ , we use the fitting formula of [Caldioli et al. \(2021\)](#). We note that directly using their fitting formula will completely erase away the  $\sim 2\text{--}3R_\oplus$  peak in our radius distribution as  $\eta \sim 1$  for our sub-Neptunes. In fact, we find that using the calculations of [Caldioli et al. \(2021\)](#), a  $5M_\oplus$  core at 0.1 au would require envelope mass fraction of  $\geq 0.1$  to survive. By contrast, [Owen & Wu \(2017\)](#) quoted threshold envelope mass fraction of  $\sim 0.01$  for survival against photoevaporative mass loss for the same planet using a fixed  $\eta = 0.1$ , and their result is the basis for the pronounced peak in the radius distribution at  $\sim 2R_\oplus$  which corresponds to an envelope mass fraction  $\sim 0.01$ .<sup>5</sup>

For the purpose of this section, we simply reduce  $\eta$  of [Caldioli et al. \(2021\)](#) by 0.1 to match the fiducial number of [Owen & Wu \(2017\)](#) while still emulating the dependence of  $\eta$  on planet properties, to assess the effect of mass loss while maintaining the existence of peaks and valleys in the radius distribution. Figure 15 illustrates how this “weak” mass loss shifts the location of the local peak in the radius distribution to a smaller value over time while filling in the  $\sim 1\text{--}1.4R_\oplus$  end of the radius valley. The shift in the radius peak is also observed if there is no mass loss; however, thermal evolution on its own would simply shrink all planets and so there is no filling-in of the radius valley.

We note that measurable changes in the observed radius distribution over time appear to be complicated by the uncertainties in age estimates. For instance, using the Gaia-Kepler catalog, [Berger et al. \(2020\)](#) find a slight shift in the radius peak and valley to smaller value at  $>1$  Gyr as well as a  $\sim 60\%$  increase in the super-Earth / sub-Neptune number ratio (see their Figure 7). By comparison, using the California-Kepler Survey, [David et al. \(2021\)](#) report no change in the location of the peak but what appears to be a shift of the location of the radius valley to larger radii over time. Our result appears to be in better agreement with the result of [Berger et al. \(2020\)](#), although we do not produce as many super-Earths given that the small planets already dominate the initial population in our models. We conclude that the main lesson to be taken from our exercise is that even photoevaporative mass loss or simple thermal evolution can produce a noticeable change to the radius distribution over multi-Gyr timescale. More definitive comparison to observations would require a larger and cleaner sample with better handle on age estimates of planetary systems as well as a broader sampling of system ages below  $\sim 1$  Gyr (e.g., [Newton et al. 2021](#)).

## 4.2 System Metallicity

Observations report a strong positive correlation between the occurrence rate of gas giants and stellar metallicity (e.g., [Fischer & Valenti 2005](#)) whereas the metallicity trend with sub-Neptune occurrence rate is significantly weaker (e.g., [Wang & Fischer 2015](#); [Petigura et al. 2018](#); [Wilson et al. 2021](#)), with hotter planets more likely to appear around metal-rich stars (e.g., [Wilson et al. 2018](#)).

In our theory of primordial gas accretion, metallicity can affect the final gas mass and the apparent radius of the planet. With all else equal, higher metallicity effects slower cooling and therefore less accretion, leading to smaller planets. Once  $Z \gtrsim 0.4$ , the trend reverses and the high mean molecular weight enhances gas accretion,

leading to larger planets. By comparison, atmospheres with larger metallicity will appear larger due to an enhanced opacity.

To see which effect dominates, we compare the expected change in radius from solar metallicity to  $50\times$  solar metallicity in number, corresponding to a change in mass ratio  $Z = 0.02$  to  $Z \sim 0.4$  (equivalently,  $\mu_{\text{env}} = 2.4$  to  $\mu_{\text{env}} = 3.6$ ). From equation 10,  $M_{\text{gas}}/M_{\text{core}} \propto Z^{-0.4} \mu_{\text{env}}^{2.2}$  and so  $M_{\text{gas}}/M_{\text{core}}$  decreases by a factor of  $\sim 0.76$ , which amounts to  $\sim 3\text{--}4\%$  decrease in radius. The same enhancement in the envelope metallicity enlarges the effective radius of the planet by  $\sim 3\%$  as well ([Lopez & Fortney 2014](#)), so changes in radii for  $50\times$  enhancement in metallicity compared to the solar value are within the current measurement uncertainties in exoplanet radius (and in this case, the two effects would cancel each other out). Sufficiently large  $Z \gtrsim 0.4$  would produce a population of larger planets; however, such high metallicity enhancement in planetary envelope is likely not the norm as it would push would-be sub-Neptunes into runaway accretion and create more gas giants ([Lee & Chiang 2016](#)), contrary to the observed ubiquity of sub-Neptunes.

What is more likely is that all else is not equal with varying stellar metallicity. Assuming the present-day metallicity enhancement over solar value of planet-hosting stars reflects the metal-enrichment of their protoplanetary disks, the more massive solid reservoir likely spawned systematically more massive cores, creating larger planets (e.g., [Dawson et al. 2015](#)). Core growth by pebble accretion is also enhanced with higher disk metallicity (e.g., [Lambrechts & Johansen 2014](#); [Lin et al. 2018](#)) and the disks may disperse later around stars in high metallicity environment (e.g., [Yasui et al. 2009](#)), allowing for the emergence of more gas-rich planets in solid-enhanced disks.

## 4.3 Dusty vs. Dust-free

In this paper, we focussed our analysis on “dust-free” accretion whereby dust grains do not contribute to the opacity of either the envelope or the underlying disk. While such scenario is not inconceivable—for instance, dust grains are expected to coagulate and rain out within planetary envelopes (e.g., [Mordasini et al. 2014](#); [Ormel 2014](#)) and within  $\sim 100$  days of orbital period, solid coagulation timescales are orders of magnitude shorter than  $\sim 10$  Myrs so that most solids are likely collected into planets—it is more useful to consider it as a limiting case. How would accounting for dust opacity change our result?

While we defer more careful study to a future project, we make a few preliminary observations here. First, from Figure 3, we see that dusty disk will be optically thick unless the disk surface density falls below 6 orders of magnitude. The midplane temperature of these optically thick disks will be dominated by accretional heating reaching temperatures  $\sim 2000$  K in the inner disk for an accretion rate of  $\sim 10^{-8} M_\odot \text{ yr}^{-1}$  (see also [Jankovic et al. 2021](#)). In hotter disks, the maximal isothermal limit will drop pushing the transition core mass between the maximal isothermal limit and the cooling curve to a larger value. Second, the slower cooling (and therefore accretion) of dusty envelopes will reduce the overall gas content of planets. Both effects would bring our model into a better agreement with the currently observed radius-mass distribution. Furthermore, with the reduction in the number of large planets, the overabundance of  $\geq 8R_\oplus$  planets in our models (Figure 11) can be removed, in better agreement with the observations.

<sup>5</sup> Using yet another fitting formula by [Kubyshkina et al. \(2018\)](#), we find that this benchmark planet would not be able to hold onto any gaseous envelope.

## 5 CONCLUSION

Using more realistic disk conditions, we demonstrated that even in the absence of mass loss (and with a single core composition), peaks and valleys in the radius distribution naturally appear from primordial gas accretion alone as the physics that limits the rate of accretion onto planetary cores switches. Light cores ( $M_{\text{core}} \lesssim 2\text{--}3M_{\oplus}$ , depending on the orbital period) reach their isothermal maximally cooled limit, unable to accrue sufficient amount of gas so that they are fated to remain as rocky terrestrials. The isothermal-to-cooling transition carves out a gap at  $\sim 1.8R_{\oplus}$  in the radius distribution. Massive cores ( $M_{\text{core}} \gtrsim 10M_{\oplus}$ ) undergo runaway accretion before being halted by global disk accretion. The cooling-to-disk transition dampens the population of planets larger than  $\gtrsim 4R_{\oplus}$ . The combination of the two effects gives rise to the radius peak at  $\sim 2\text{--}3R_{\oplus}$ , as observed.

Accounting for these limits and transitions on gas mass allows for the underlying core mass distribution to be broad and even bottom-heavy extending to sub-Earth masses so that both the rise in the occurrence rate of sub-Earth sized planets and the location of the radius valley (Hsu et al. 2019) can be reproduced. Our model further reproduces the shape of the radius valley in the radius-period space, with the slope  $R_{\text{gap}} \propto P^{-0.11}$  for top-heavy and  $R_{\text{gap}} \propto P^{-0.10}$  for bottom-heavy core mass distributions, in good agreement with that observed (Van Eylen et al. 2018; Martinez et al. 2019). We are also able to reproduce the rise in the gap radius with stellar mass  $R_{\text{gap}} \propto M_{\star}^{0.24}$  for top-heavy and  $R_{\text{gap}} \propto M_{\star}^{0.21}$  for bottom-heavy core mass distributions, both of which agree with the data (Berger et al. 2020) within  $1\text{--}\sigma$ .

Most of the planets with both mass and radii measurements appear to fall within the parameter space (total mass  $\sim 6\text{--}20M_{\oplus}$  and radii  $\sim 2\text{--}4R_{\oplus}$ ) that should be sparsely populated. While it is possible that with more mass measurements, we may find more planets that are in better agreement with the model presented here, we reiterate some limitations of the model that once addressed may alleviate this apparent disagreement. First, we adopted a universal core mass distribution that is invariant with orbital period with no relationship between the mass and the assembly time. Second, we limited our discussion to dust-free opacities which affect both the disk temperature and the rate of gas accretion onto planetary cores. Adopting dusty opacities may change considerably the expected planet population. Third, we assumed a single core composition. It may indeed be that at least some of the planets that comprise the  $2\text{--}3R_{\oplus}$  peak in the radius distribution have more icy cores.

We close by listing potential observational tests. First, since it is likely that some degree of mass loss is sculpting the radius distribution within short orbital periods ( $\lesssim 30$  days) over Gyrs, one of the more immediate tests that can be performed is to constrain the occurrence rate of Earths and super-Earths at longer orbital periods. If mass loss is the original and the dominant mechanism to carve out the radius valley, then we should expect significantly less super-Earths and their smaller counterparts beyond  $\sim 30$  days. If on the other hand there is no strong or obvious sign of a drop in their occurrence rate beyond  $\sim 30$  days, then gas accretion may well be the origin of the radius gap. Hsu et al. (2019) suggest that these small planets continue to dominate the total population at these long orbital periods while Wilson et al. (2021) report a very slight decrease. These planets are exactly at the edge of the detection limit afforded by *Kepler* dataset so for more definitive measurements, we would have to wait for PLATO.

Second, Roman Space Telescope promises to probe the bottom of the planetary mass function at a few 100 days, with a caveat that the microlensing host stars are most likely M dwarfs. A broad mass distribution that extends to sub-Earth masses would give more

credence to our model, while keeping in mind that a more peaked distribution does not necessarily rule out primordial radius gap so long as it samples core masses below those whose gas masses are expected to be limited by the maximal isothermal limit.

Finally, as we enlarge the sample of detected planets around cooler stars ( $M_{\star} \lesssim 0.4M_{\odot}$ ), any sign of weaker trend between the radius gap and stellar mass would be in support of the primordial origin as long as such features are not erased by mass loss processes. Again, it would be useful to test these dependencies at orbital periods beyond  $\sim 30$  days where mass loss largely halts.

## ACKNOWLEDGEMENTS

We thank Eugene Chiang for helpful discussion on disk structures. E.J.L. gratefully acknowledges support from NSERC, FRQNT, the McGill Space Institute, and the William Dawson Scholarship from McGill. A.K. was supported by the Faculty of Science Undergraduate Research Award from McGill and by the Technologies for Exoplanetary Science CREATE program. D.P.T. acknowledges support by the Trottier Fellowship from the Exoplanet Research Institute (iREx). This research has made use of the NASA Exoplanet Archive, which is operated by the California Institute of Technology, under contract with the National Aeronautics and Space Administration under the Exoplanet Exploration Program.

## DATA AVAILABILITY

The data underlying this article will be shared on reasonable request to the corresponding author.

## REFERENCES

- Ali-Dib M., Cumming A., Lin D. N. C., 2020, *MNRAS*, **494**, 2440
- Berger T. A., Huber D., Gaidos E., van Saders J. L., Weiss L. M., 2020, *AJ*, **160**, 108
- Béthune W., Rafikov R. R., 2019, *MNRAS*, **488**, 2365
- Bitsch B., Morbidelli A., Johansen A., Lega E., Lambrechts M., Crida A., 2018, *A&A*, **612**, A30
- Burke C. J., et al., 2015, *ApJ*, **809**, 8
- Caldirola A., Haardt F., Gallo E., Spinelli R., Malsky I., Rauscher E., 2021, arXiv e-prints, p. arXiv:2112.00744
- Chabrier G., Mazevet S., Soubiran F., 2019, *The Astrophysical Journal*, **872**, 51
- Chiang E. I., Goldreich P., 1997, *ApJ*, **490**, 368
- Chiang E., Laughlin G., 2013, *MNRAS*, **431**, 3444
- Chiang E. I., Joungh M. K., Creech-Eakman M. J., Qi C., Kessler J. E., Blake G. A., van Dishoeck E. F., 2001, *ApJ*, **547**, 1077
- Choksi N., Chiang E., 2020, *MNRAS*, **495**, 4192
- David T. J., et al., 2021, *AJ*, **161**, 265
- Dawson R. I., Chiang E., Lee E. J., 2015, *MNRAS*, **453**, 1471
- Dorn C., Harrison J. H. D., Bonsor A., Hands T. O., 2019, *MNRAS*, **484**, 712
- Duffell P. C., MacFadyen A. I., 2013, *ApJ*, **769**, 41
- Ferguson J. W., Alexander D. R., Allard F., Barman T., Bodnarik J. G., Hauschildt P. H., Heffner-Wong A., Tamanai A., 2005, *ApJ*, **623**, 585
- Fischer D. A., Valenti J., 2005, *ApJ*, **622**, 1102
- Flaherty K. M., et al., 2017, *ApJ*, **843**, 150
- Flaherty K., et al., 2020, *ApJ*, **895**, 109
- Foreman-Mackey D., Hogg D. W., Lang D., Goodman J., 2013, *PASP*, **125**, 306
- Fortney J. J., Marley M. S., Barnes J. W., 2007, *The Astrophysical Journal*, **659**, 1661

- Freedman R. S., Lustig-Yaeger J., Fortney J. J., Lupu R. E., Marley M. S., Lodders K., 2014, *ApJS*, **214**, 25
- Fressin F., et al., 2013, *ApJ*, **766**, 81
- Fulton B. J., Petigura E. A., 2018, *AJ*, **156**, 264
- Fulton B. J., et al., 2017, *AJ*, **154**, 109
- Fung J., Shi J.-M., Chiang E., 2014, *ApJ*, **782**, 88
- Fung J., Zhu Z., Chiang E., 2019, *ApJ*, **887**, 152
- Gaia Collaboration et al., 2018, *A&A*, **616**, A1
- Gao P., Zhang X., 2020, *ApJ*, **890**, 93
- Garaud P., Lin D. N. C., 2007, *ApJ*, **654**, 606
- Ginzburg S., Chiang E., 2019, *MNRAS*, **487**, 681
- Ginzburg S., Schlichting H. E., Sari R., 2018, *MNRAS*, **476**, 759
- Grevesse N., Noels A., 1993, *Origin and Evolution of the Elements*. Cambridge University Press
- Güdel M., et al., 2007, *A&A*, **468**, 353
- Gupta A., Schlichting H. E., 2019, *MNRAS*, **487**, 24
- Hallatt T., Lee E. J., 2022, *ApJ*, **924**, 9
- Hartmann L., Calvet N., Gullbring E., D'Alessio P., 1998, *ApJ*, **495**, 385
- Hsu D. C., Ford E. B., Ragozzine D., Morehead R. C., 2018, *AJ*, **155**, 205
- Hsu D. C., Ford E. B., Ragozzine D., Ashby K., 2019, *AJ*, **158**, 109
- Jankovic M. R., Owen J. E., Mohanty S., Tan J. C., 2021, *MNRAS*, **504**, 280
- Johnstone C. P., Bartel M., Güdel M., 2021, *A&A*, **649**, A96
- King G. W., Wheatley P. J., 2021, *MNRAS*, **501**, L28
- Kite E. S., Fegley Bruce J., Schaefer L., Ford E. B., 2019, *ApJ*, **887**, L33
- Kominami J., Ida S., 2002, *Icarus*, **157**, 43
- Kubyskhina D., et al., 2018, *ApJ*, **866**, L18
- Lambrechts M., Johansen A., 2014, *A&A*, **572**, A107
- Lambrechts M., Lega E., 2017, *A&A*, **606**, A146
- Lee E. J., 2019, *ApJ*, **878**, 36
- Lee E. J., Chiang E., 2015, *ApJ*, **811**, 41
- Lee E. J., Chiang E., 2016, *ApJ*, **817**, 90
- Lee E. J., Chiang E., 2017, *ApJ*, **842**, 40
- Lee E. J., Connors N. J., 2021, *ApJ*, **908**, 32
- Lee E. J., Chiang E., Ormel C. W., 2014, *ApJ*, **797**, 95
- Lee E. J., Chiang E., Ferguson J. W., 2018, *MNRAS*, **476**, 2199
- Libby-Roberts J. E., et al., 2020, *AJ*, **159**, 57
- Lin J. W., Lee E. J., Chiang E., 2018, *MNRAS*, **480**, 4338
- Lopez E. D., Fortney J. J., 2014, *ApJ*, **792**, 1
- Lloyd R. O. P., Shkolnik E. L., Schneider A. C., Richey-Yowell T., Barman T. S., Peacock S., Pagano I., 2020, *ApJ*, **890**, 23
- Lubow S. H., D'Angelo G., 2006, *ApJ*, **641**, 526
- Lynden-Bell D., Pringle J. E., 1974, *MNRAS*, **168**, 603
- Lyon S. P., Johnson J. D., 1992, Technical Report LA-UR-92-3407, SESAME: The Los Alamos National Laboratory Equation of State Database.. Los Alamos National Laboratory
- Mamajek E. E., 2009, in Usuda T., Tamura M., Ishii M., eds, *American Institute of Physics Conference Series Vol. 1158, Exoplanets and Disks: Their Formation and Diversity*. pp 3–10 ([arXiv:0906.5011](https://arxiv.org/abs/0906.5011)), [doi:10.1063/1.3215910](https://doi.org/10.1063/1.3215910)
- Marcy G. W., et al., 2014, *ApJS*, **210**, 20
- Martinez C. F., Cunha K., Ghezzi L., Smith V. V., 2019, *ApJ*, **875**, 29
- Michel A., van der Marel N., Matthews B., 2021, arXiv e-prints, [p. arXiv:2104.05894](https://arxiv.org/abs/2104.05894)
- Moldenhauer T. W., Kuiper R., Kley W., Ormel C. W., 2021, *A&A*, **646**, L11
- Mordasini C., Klahr H., Alibert Y., Miller N., Henning T., 2014, *A&A*, **566**, A141
- Mulders G. D., Pascucci I., Apai D., 2015, *ApJ*, **798**, 112
- Newton E. R., et al., 2021, *AJ*, **161**, 65
- Ormel C. W., 2014, *ApJ*, **789**, L18
- Owen J. E., Adams F. C., 2019, *MNRAS*, **490**, 15
- Owen J. E., Jackson A. P., 2012, *MNRAS*, **425**, 2931
- Owen J. E., Wu Y., 2013, *ApJ*, **775**, 105
- Owen J. E., Wu Y., 2017, *ApJ*, **847**, 29
- Owen J. E., Ercolano B., Clarke C. J., Alexander R. D., 2010, *MNRAS*, **401**, 1415
- Owen J. E., Ercolano B., Clarke C. J., 2011, *MNRAS*, **412**, 13
- Petigura E. A., Marcy G. W., Howard A. W., 2013, *ApJ*, **770**, 69
- Petigura E. A., et al., 2017, *AJ*, **154**, 107
- Petigura E. A., et al., 2018, *AJ*, **155**, 89
- Piro A. L., Vissapragada S., 2020, *AJ*, **159**, 131
- Pollack J. B., Hubickyj O., Bodenheimer P., Lissauer J. J., Podolak M., Greenzweig Y., 1996, *Icarus*, **124**, 62
- Rogers L. A., 2015, *ApJ*, **801**, 41
- Rogers J. G., Owen J. E., 2021, *MNRAS*, **503**, 1526
- Rogers L. A., Seager S., 2010, *ApJ*, **712**, 974
- Rogers J. G., Gupta A., Owen J. E., Schlichting H. E., 2021, arXiv e-prints, [p. arXiv:2105.03443](https://arxiv.org/abs/2105.03443)
- Rosenthal M. M., Chiang E. I., Ginzburg S., Murray-Clay R. A., 2020, *MNRAS*, **498**, 2054
- Tanigawa T., Tanaka H., 2016, *ApJ*, **823**, 48
- Thompson S., 1990, *ANEOS Analytic Equations of State for Shock Physics Codes Input Manual*
- Thorngren D. P., Fortney J. J., Murray-Clay R. A., Lopez E. D., 2016, *The Astrophysical Journal*, **831**, 64
- Valencia D., O'Connell R. J., Sasselov D., 2006, *Icarus*, **181**, 545
- Van Eylen V., Agentoft C., Lundkvist M. S., Kjeldsen H., Owen J. E., Fulton B. J., Petigura E., Snellen I., 2018, *MNRAS*, **479**, 4786
- Venturini J., Guilera O. M., Haldemann J., Ronco M. P., Mordasini C., 2020, *A&A*, **643**, L1
- Wang J., Fischer D. A., 2015, *AJ*, **149**, 14
- Wilson R. F., et al., 2018, *AJ*, **155**, 68
- Wilson R. F., et al., 2021, arXiv e-prints, [p. arXiv:2111.01753](https://arxiv.org/abs/2111.01753)
- Wu Y., 2019, *ApJ*, **874**, 91
- Yasui C., Kobayashi N., Tokunaga A. T., Saito M., Tokoku C., 2009, *ApJ*, **705**, 54
- Youdin A. N., 2011, *ApJ*, **742**, 38
- Zeng L., et al., 2019, *Proceedings of the National Academy of Science*, **116**, 9723
- Zhu W., Dong S., 2021, *ARA&A*, **59**
- Zhu W., Petrovich C., Wu Y., Dong S., Xie J., 2018, *ApJ*, **860**, 101

This paper has been typeset from a  $\text{\LaTeX}$  file prepared by the author.